

E-PINNs: EPISTEMIC PHYSICS-INFORMED NEURAL NETWORKS

✉ **Bruno Jacob**

Pacific Northwest National Laboratory
Richland, WA 99354
bruno.jacob@pnnl.gov

✉ **Ashish S. Nair**

University of Notre Dame
South Bend, IN 46637
anair@nd.edu

✉ **Amanda A. Howard**

Pacific Northwest National Laboratory
Richland, WA 99354
amanda.howard@pnnl.gov

✉ **Jan Drgona**

Pacific Northwest National Laboratory
Richland, WA 99354
jan.drgona@pnnl.gov

✉ **Panos Stinis**

Pacific Northwest National Laboratory
Richland, WA 99354
panagiotis.stinis@pnnl.gov

November 14, 2025

ABSTRACT

Physics-informed neural networks (PINNs) have demonstrated promise as a framework for solving forward and inverse problems involving partial differential equations. Despite recent progress in the field, it remains challenging to quantify uncertainty in these networks. While techniques such as Bayesian PINNs (B-PINNs) provide a principled approach to capturing epistemic uncertainty through Bayesian inference, they can be computationally expensive for large-scale applications. In this work, we propose Epistemic Physics-Informed Neural Networks (E-PINNs), a framework that uses a small network, the *epinet*, to efficiently quantify epistemic uncertainty in PINNs. The proposed approach works as an add-on to existing, pre-trained PINNs with a small computational overhead. We demonstrate the applicability of the proposed framework in various test cases and compare the results with B-PINNs using Hamiltonian Monte Carlo (HMC) posterior estimation and dropout-equipped PINNs (Dropout-PINNs). In our experiments, E-PINNs achieve calibrated coverage with competitive sharpness at substantially lower cost. We demonstrate that when B-PINNs produce narrower bands, they under-cover in our tests. E-PINNs also show better calibration than Dropout-PINNs in these examples, indicating a favorable accuracy-efficiency trade-off.

Keywords Physics-informed neural networks · Uncertainty quantification · Epistemic neural networks

1 Introduction

Uncertainty quantification is a critical component in the deployment of machine learning models for scientific and engineering applications. Physics-Informed Neural Networks (PINNs) have shown promise in solving partial differential equations (PDEs) by incorporating physical laws directly into the learning process [1]. PINNs have been successfully applied to a diverse range of scientific and engineering problems, including fluid dynamics and turbulence [2, 3, 4, 5], heat transfer [6, 7, 8, 9], biomedical applications [10, 11, 12], electromagnetic systems [13, 14], among many other applications. When employing neural networks to physics-informed tasks, it is crucial to ensure that the models are not only accurate but also provide insights into the confidence of their predictions. However, traditional PINNs do not inherently quantify uncertainty [15].

Uncertainty is typically classified into two types: aleatoric or epistemic uncertainty. Aleatoric refers to the uncertainty inherent in the data, often due to noise or stochasticity in the physical process being modeled. This type of uncertainty cannot be reduced by collecting more data. In contrast, epistemic uncertainty arises due to limited data or lack of knowledge about the model itself and can be reduced with more data or a better model [16, 17]. Understanding and distinguishing between these types of uncertainty is crucial for robust modeling, particularly in scientific applications where decision-making based on model predictions can have significant consequences.

Classical uncertainty quantification techniques for parametric PDEs, such as polynomial chaos expansion (PCE) [18, 19], have been widely used for forward propagation of parametric uncertainty and surrogate modeling. These methods expand solutions in orthogonal polynomials of random input parameters and, with sparsity and dimension reduction, can address high-dimensional inputs more efficiently. Recent developments have incorporated physics constraints into PCE-based surrogates [19], reducing model evaluations and promoting physically consistent predictions. These approaches typically assume sufficiently smooth responses and a prescribed set of random input parameters. By design, PCE propagates parametric uncertainty through known PDE operators; it does not address epistemic uncertainty in learned PDE surrogates that arises from limited data and model capacity.

The field of uncertainty quantification in deep learning has seen substantial growth in recent years. Bayesian Neural Networks (BNNs) provide a principled approach to uncertainty quantification by placing prior distributions over model parameters and inferring posterior distributions through Bayesian inference [20, 21, 22, 23]. However, they often face scalability challenges when applied to complex models or high-dimensional data [24].

Ensemble methods represent another prominent approach to uncertainty quantification, where multiple models are trained, and their predictions aggregated to estimate uncertainty [25]. While effective in practice, these methods can be computationally expensive as they require training multiple independent models. Deep ensembles, in particular, have demonstrated strong performance in capturing uncertainty by training neural networks with different random initializations [26]. However, previous studies have shown that naively pooling ensemble predictions can sometimes lead to under-confidence in the model’s predictions [27].

As an alternative to the computationally intensive Bayesian and ensemble methods, dropout methods offer a computationally lighter approach for uncertainty quantification. Dropout approximates Bayesian inference through random deactivation of neurons during both training and inference, effectively sampling from a posterior distribution over the network parameters without explicitly performing Bayesian sampling [28, 29, 30, 31]. This method has been widely adopted due to its simplicity and effectiveness, although its theoretical underpinnings and optimal configuration remain areas of active research [32].

In the context of scientific machine learning, recent approaches have focused on integrating physical principles into the uncertainty quantification process. Physics-informed Bayesian Neural Networks have been proposed to combine the expressiveness of neural networks with the physical constraints imposed by governing equations [33, 34]. These methods aim to respect physical laws while providing probabilistic predictions, though they often face challenges related to the balance between data-driven learning and physical consistency. For PINNs [1] specifically, several uncertainty quantification methods have been developed. Bayesian PINNs (B-PINNs) incorporate prior knowledge about physical systems while quantifying both aleatoric and epistemic uncertainties through a principled Bayesian treatment [15]. However, they often struggle with scalability due to the high computational cost of sampling from the posterior distribution over the model parameters, and may suffer from high variance in the predictive distribution, particularly in high-dimensional spaces or when data is sparse [35].

Dropout has also been applied to PINNs (Dropout-PINNs), providing a more computationally efficient alternative to B-PINNs [35, 15]. However, the choice of dropout rate significantly impacts the quality of uncertainty quantification, which may limit the applicability of Dropout-PINNs in scenarios involving complex physical phenomena or sparse training data [15].

In the broader context of operator learning, uncertainty quantification for neural operators, including deep operator networks (DeepONets) [36], has gained attention. These models aim to learn mappings between function spaces. Approaches such as randomized prior methods [37], ensemble methods [38], and Bayesian formulations [39, 40] have been proposed to quantify uncertainty in operator learning settings. These methods are particularly important when the input-output mappings are complex or when dealing with noisy or incomplete data.

A recent promising direction involves combining conformal prediction methods with PINNs [41] and DeepONets [42]. Conformal methods construct distribution-free uncertainty intervals that offer rigorous finite-sample coverage guarantees without relying on Bayesian assumptions or computationally intensive sampling. For example, conformalized DeepONets utilize split conformal prediction to generate robust confidence intervals directly from neural operator predictions [42]. However, both approaches inherit fundamental conformal prediction limitations: they require representative calibration datasets that match future test distributions, and they sacrifice some training data for the calibration process [43].

1.1 Contributions and Novelty of the Present Work

In the present work, we propose epistemic physics-informed neural networks (E-PINNs), a novel extension of the traditional PINN framework designed to quantify epistemic uncertainty. Our approach builds upon the concept of

epistemic neural networks [44], which provides a flexible framework for modeling uncertainty by introducing a source of randomness into the model parameters or inputs. We provide comprehensive empirical evaluations comparing E-PINNs with B-PINNs and Dropout-PINNs on forward initial-boundary value problems and an inverse problem. Additionally, we conduct ablation studies investigating the sensitivity of E-PINNs to various hyperparameters including network size, number of training epochs and magnitude of noise. These analyses provide insights into the robustness and practical applicability of our approach.

The key innovation of our E-PINN framework lies in its architecture: we augment a base PINN with an epinet, a neural network that takes random perturbations alongside features from the base model as input. This design offers several advantages over existing methods. First, E-PINNs maintain computational efficiency even for complex models; unlike B-PINNs, which face scalability challenges when sampling from high-dimensional posterior distributions. Second, unlike dropout-based methods that randomly deactivate neurons throughout the network, our approach introduces uncertainty through a dedicated architectural component that can be trained separately from the base model, thus enabling uncertainty quantification as a post-processing step. This latter capability is particularly valuable for practitioners who already have trained PINNs and wish to add uncertainty quantification without retraining the entire model, while introducing only a small computational overhead.

This work is organized as follows: In Section 2, we present three frameworks for uncertainty quantification in PINNs: B-PINNs, Dropout-PINNs and E-PINNs. In Section 3, we report results grouped into forward problems, inverse problems, and an ablation study. Finally, a summary of the findings is presented in Section 4.

2 Methods

In this section, we detail the methodologies employed for uncertainty quantification in PINNs. We explore three primary approaches: B-PINNs, Dropout-PINNs and E-PINNs. Each method offers distinct mechanisms for capturing and quantifying uncertainty in model predictions.

In all methods, we consider a general PDE of the form

$$\mathcal{N}_x(u; \boldsymbol{\lambda}) = f(x), \quad x \in \Omega, \quad (1a)$$

$$\mathcal{B}_x(u; \boldsymbol{\lambda}) = b(x), \quad x \in \partial\Omega, \quad (1b)$$

where \mathcal{N}_x represents a general differential operator, \mathcal{B}_x denotes a general boundary operator, $u(x)$ is the solution to the PDE, $\boldsymbol{\lambda}$ is the (possibly vector-valued) set of PDE parameters, $f(x)$ is a source term, and $b(x)$ specifies the boundary conditions. The domain $\Omega \subset \mathbb{R}^d$ is a d -dimensional spatial domain, and $\partial\Omega$ denotes its boundary.

2.1 Bayesian physics-informed neural networks

B-PINNs [15] extend the traditional PINN framework by incorporating BNNs [20, 22] to quantify uncertainty in the model predictions. This approach treats the neural network parameters as random variables with specified prior distributions, allowing for the estimation of posterior distributions given observed data and physical constraints [15, 45, 46, 47].

In this framework, the solution $u(x)$ is approximated by a surrogate model $u_\theta(x)$, where θ denotes the neural network parameters, with a prior $P(\theta)$. Following the original B-PINN formulation, we evaluate the physics operators on the surrogate, i.e., $\mathcal{N}_x(u_\theta(x); \boldsymbol{\lambda})$ and $\mathcal{B}_x(u_\theta(x); \boldsymbol{\lambda})$, and compare them to (noisy) measurements when available. For readability we occasionally use residual shorthands $r_\theta(x) = \mathcal{N}_x(u_\theta(x); \boldsymbol{\lambda}) - f(x)$ and $g_\theta(x) = \mathcal{B}_x(u_\theta(x); \boldsymbol{\lambda}) - b(x)$.

We assume a dataset \mathcal{D} containing independently distributed noisy measurements of u , f , and b , denoted as $\mathcal{D} = \mathcal{D}_u \cup \mathcal{D}_f \cup \mathcal{D}_b$, where

$$\mathcal{D}_u = \{(x_i^u, \bar{u}_i)\}_{i=1}^{N_u}, \quad \bar{u}_i = u(x_i^u) + \epsilon_i^u, \quad (2a)$$

$$\mathcal{D}_f = \{(x_i^f, \bar{f}_i)\}_{i=1}^{N_f}, \quad \bar{f}_i = f(x_i^f) + \epsilon_i^f, \quad (2b)$$

$$\mathcal{D}_b = \{(x_i^b, \bar{b}_i)\}_{i=1}^{N_b}, \quad \bar{b}_i = b(x_i^b) + \epsilon_i^b, \quad (2c)$$

and N_u, N_f, N_b denote the number of measurements, and $\epsilon_i^u, \epsilon_i^f, \epsilon_i^b$ are independent Gaussian noises with zero mean and known standard deviations $\sigma_i^u, \sigma_i^f, \sigma_i^b$, i.e., $\epsilon_i^u \sim \mathcal{N}(0, (\sigma_i^u)^2)$, $\epsilon_i^f \sim \mathcal{N}(0, (\sigma_i^f)^2)$, and $\epsilon_i^b \sim \mathcal{N}(0, (\sigma_i^b)^2)$.

In general, with independent Gaussian noise on the available sensors, the unnormalized likelihood factorizes as

$$P(\mathcal{D} \mid \theta) \propto P(\mathcal{D}_u \mid \theta) P(\mathcal{D}_f \mid \theta) P(\mathcal{D}_b \mid \theta), \quad (3)$$

with

$$\ln P(\mathcal{D}_u \mid \theta) = -\frac{1}{2} \sum_{i=1}^{N_u} \frac{(u_\theta(x_i^u) - \bar{u}_i)^2}{(\sigma_i^u)^2} + \text{const}, \quad (4a)$$

$$\ln P(\mathcal{D}_f \mid \theta) = -\frac{1}{2} \sum_{i=1}^{N_f} \frac{(\mathcal{N}_x(u_\theta(x_i^f); \boldsymbol{\lambda}) - \bar{f}_i)^2}{(\sigma_i^f)^2} + \text{const}, \quad (4b)$$

$$\ln P(\mathcal{D}_b \mid \theta) = -\frac{1}{2} \sum_{i=1}^{N_b} \frac{(\mathcal{B}_x(u_\theta(x_i^b); \boldsymbol{\lambda}) - \bar{b}_i)^2}{(\sigma_i^b)^2} + \text{const}. \quad (4c)$$

If a subset of sensors is unavailable (e.g., no f measurements), the corresponding factor is omitted. In the present work, we add observation noise only to interior u measurements; we do not add noise to f or to boundary values when generating data. In our B-PINN experiments all available channels are modeled with Gaussian likelihoods: the u -data likelihood uses the known noise level, and the physics and boundary residual channels use small fixed noise levels for HMC stability. Unless otherwise noted, we set this residual noise standard deviation to 0.01. We report B-PINN results for the cases indicated in Section 3.

With a prior $P(\theta)$ on network parameters and the data likelihood $P(\mathcal{D} \mid \theta)$ defined above, Bayes' theorem gives the posterior:

$$P(\theta \mid \mathcal{D}) \propto P(\mathcal{D} \mid \theta) P(\theta), \quad (5)$$

where $P(\mathcal{D})$ denotes the marginal likelihood, often intractable to compute directly. For inverse problems with unknown PDE parameters $\boldsymbol{\lambda}$, we place a prior $P(\boldsymbol{\lambda})$ and infer the joint posterior

$$P(\theta, \boldsymbol{\lambda} \mid \mathcal{D}) \propto P(\mathcal{D} \mid \theta, \boldsymbol{\lambda}) P(\theta) P(\boldsymbol{\lambda}). \quad (6)$$

Sampling or approximation methods (e.g., Hamiltonian Monte Carlo, variational inference) can then be employed to approximate the posterior distribution. We draw weight samples $\theta^{(i)} \sim P(\theta \mid \mathcal{D})$ (or joint samples $(\theta^{(i)}, \boldsymbol{\lambda}^{(i)})$) and compute *posterior predictive* realizations $u_{\theta^{(i)}}(x)$.

This Bayesian formulation captures both aleatoric (through sensor noise) and epistemic (through the posterior over θ) uncertainty. In our experiments we do not inject noise at prediction time; as a result, the reported predictive bands reflect *epistemic* variability only, i.e., u noise enters only through the likelihood during training. Given the low performance of B-PINN-VI reported by [15], in this work we will use only B-PINN-HMC when referring to B-PINNs in the tests and comparisons presented in Section 3.

2.2 Dropout-based physics-informed neural networks

Dropout-PINNs incorporate dropout layers within the neural network architecture as a means to quantify uncertainty [35]. In general, Monte Carlo dropout can reflect aspects of total uncertainty; however, in this paper we report *epistemic-only* uncertainty, i.e., the variability induced by stochastic dropout masks with no additive observation noise at prediction time. Dropout, originally introduced as a regularization technique to prevent overfitting [48], randomly deactivates a subset of neurons during training, effectively sampling from an ensemble of sub-networks.

In the context of PINNs, dropout is applied during both training and inference phases. During training, it regularizes the network by preventing co-adaptation of neurons, while during inference, it enables uncertainty quantification through Monte Carlo sampling. By performing multiple forward passes with different dropout masks, one can obtain a distribution of predictions that reflects the uncertainty in the model's output. The predictive mean and variance are then computed as:

$$\mathbb{E}[u_\theta(x)] = \frac{1}{M} \sum_{m=1}^M u_{\theta^{(m)}}(x), \quad (7a)$$

$$\text{Var}[u_\theta(x)] = \frac{1}{M} \sum_{m=1}^M (u_{\theta^{(m)}}(x) - \mathbb{E}[u_\theta(x)])^2, \quad (7b)$$

where $u_{\theta^{(m)}}$ denotes the output of the model's m -th forward pass, $\theta^{(m)}$ represents the network parameters sampled with dropout for the m -th forward pass, and M is the total number of Monte Carlo samples.

While dropout provides a computationally efficient method for uncertainty quantification, it has inherent limitations. As reported in [15], the choice of dropout rate significantly influences the quality of the uncertainty estimates, with higher

rates potentially leading to underconfident predictions and lower rates risking overfitting [29]. Moreover, dropout-based methods do not adequately represent the full uncertainty spectrum, especially in regions with sparse or no training data [15, 49].

Nevertheless, when compared to Bayesian approaches like B-PINNs, dropout-based methods offer a simpler implementation with lower computational overhead. The method requires minimal modifications to the existing PINN architecture and can be easily integrated into existing frameworks. Furthermore, the computational cost of uncertainty estimation scales linearly with the number of Monte Carlo samples M , making it particularly attractive for large-scale applications where full Bayesian inference might be computationally prohibitive. In Section 3, we use dropout to compare the quality of uncertainty and computational time in various examples.

2.3 Epistemic physics-informed neural networks

Epistemic neural networks are a generalization of ensemble-based uncertainty estimation methods proposed by [44]. This framework defines a parameterized function u , approximated by a neural network with learnable parameters θ as u_θ , and a reference distribution P_z , typically chosen as a standard normal distribution $\mathcal{N}(0, I)$. An *epistemic index*, denoted by z , is sampled from P_z and used to express the uncertainty of u . Thus, for an input x and epistemic index z , we obtain a realization of the output, $u_\theta(x, z)$.

In the present work, we introduce epistemic PINNs (E-PINNs): a modification of the original PINN architecture that supplements the base PINN with an *epinet*, a companion neural network designed to quantify uncertainty in the base network. A diagram of the framework is shown in Fig. 1, and a pseudocode of the algorithm is shown in Algorithm 1.

Formally, given an input feature x and an epistemic index $z \sim P_z$, the E-PINN prediction is given by:

$$\underbrace{u_\theta(x, z)}_{\text{E-PINN output}} = \underbrace{u_\xi(x)}_{\text{base PINN output}} + \underbrace{e_\eta(\tilde{x}, z)}_{\text{epinet output}}, \quad (8)$$

where $u_\xi(x)$ is the output of the base PINN with trainable parameters ξ , and $e_\eta(\tilde{x}, z)$ is the output of the epinet. We decompose the epinet as a trainable component with parameters η^L and a frozen prior component with parameters η^P (not trained). The set of trainable parameters is $\theta = (\xi, \eta^L)$. Throughout this work we adopt a decoupled training procedure: a base PINN is pre-trained and then held fixed while the epinet is trained. We define the augmented feature vector

$$\tilde{x} \equiv \text{sg}([x, h_{\text{penultimate}}(x; \xi)]) \in \mathbb{R}^{d_x + H_{\text{base}}},$$

where $h_{\text{penultimate}}(x; \xi)$ are the last hidden-layer activations of the base PINN and sg denotes a stop-gradient operator that blocks backpropagation from the epinet to the base network.

The epinet consists of two components: a learnable network, with output $e_{\eta^L}^L(\tilde{x}, z)$, and a prior network with frozen weights, with output $e^P(\tilde{x}, z)$. Specifically, given inputs \tilde{x} and epistemic index z , the output of the epinet is:

$$e_\eta(\tilde{x}, z) = e_{\eta^L}^L(\tilde{x}, z) + \alpha e^P(\tilde{x}, z), \quad (9)$$

where α is a hyperparameter used to scale the effect of the prior epinet. In the experiments we treat α as a tunable scalar and, unless stated otherwise, set $\alpha = 0.05$. We design e^P as a multilayer perceptron (MLP) with initial weights and biases computed using Xavier initialization; its parameters η^P remain frozen during training and are not learned. Unless stated otherwise, $z \sim \mathcal{N}(0, I_{d_z})$ with default $d_z = 8$.

Intuitively, the two-component epinet design can be understood through the lens of corruption and correction. The frozen prior network e^P , with its randomly initialized weights, introduces a form of stochastic perturbation to the deterministic base PINN prediction, essentially acting as a source of epistemic variability that prevents the model from collapsing to overconfident predictions. The trainable network $e_{\eta^L}^L$ then learns to correct and calibrate this baseline variability by adapting to the observed data and physics constraints. The choice of initialization distribution for e^P (Xavier, He, orthogonal, etc.) implicitly determines the prior structure of the epistemic uncertainty, with different distributions yielding different baseline uncertainty patterns.

The E-PINN framework quantifies uncertainty through Monte Carlo sampling over the epistemic index z . For uncertainty estimation, we sample multiple realizations z_1, z_2, \dots, z_M from P_z and compute the corresponding

predictions $u_\theta(x, z_i)$. The mean prediction and the epistemic uncertainty are then computed as:

$$\mu_u(x) = \mathbb{E}_Z[u_\theta(x, Z)] \approx \frac{1}{M} \sum_{i=1}^M u_\theta(x, z_i), \quad (10a)$$

$$\sigma_u^2(x) = \text{Var}_Z[u_\theta(x, Z)] \approx \frac{1}{M} \sum_{i=1}^M (u_\theta(x, z_i) - \mu_u(x))^2, \quad (10b)$$

where $Z \sim P_z$ is the epistemic index and $\{z_i\}_{i=1}^M$ are Monte Carlo samples. This approach provides a computationally efficient method for uncertainty quantification that captures the variability in model predictions due to the stochastic nature of the epistemic index.

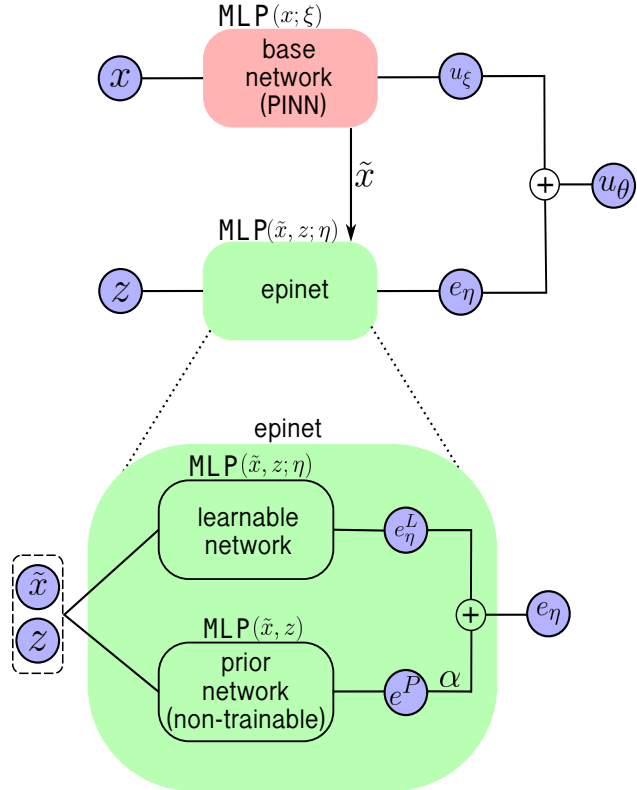


Figure 1: Schematic diagram of the E-PINN architecture. The base PINN (red) produces a deterministic prediction u_ξ . The epinet (green) receives as input the augmented feature vector $\tilde{x} = \text{sg}([x, h_{\text{penultimate}}(x; \xi)])$, where sg blocks gradients to the base network, together with a random epistemic index $z \sim P_z$. Internally, the epinet comprises two neural networks: a trainable network producing e_η^L and a non-trainable prior network with fixed parameters producing e_η^P . The final epinet output is $e_\eta = e_\eta^L + \alpha e_\eta^P$, a weighted sum controlled by the hyperparameter α . The sum of the epinet output and the base PINN output yields the stochastic E-PINN prediction u_θ .

2.4 Loss function and training

For the optimization-based approaches in this paper (Dropout-PINN and E-PINN), the underlying training process involves minimizing a composite loss function that incorporates both data observations and physical constraints:

$$\mathcal{L}_{\text{total}} = w_{\text{data}} \mathcal{L}_{\text{data}} + w_{\text{pde}} \mathcal{L}_{\text{pde}} + w_{\text{bc}} \mathcal{L}_{\text{boundary}}, \quad (11)$$

where w_{data} , w_{pde} , and w_{bc} are weighting coefficients that balance the different components of the loss, and:

Algorithm 1 Epistemic Physics-Informed Neural Networks (E-PINNs)

Require:

```

1: PDE operators  $\mathcal{N}_x$ ,  $\mathcal{B}_x$ , and parameters  $\lambda$ 
2: Training data  $\{(x_i^u, \bar{u}_i)\}_{i=1}^{N_u}$ ,  $\{(x_i^f, \bar{f}_i)\}_{i=1}^{N_f}$ ,  $\{(x_i^b, \bar{b}_i)\}_{i=1}^{N_b}$ 
3: Reference distribution  $P_z$  for epistemic index sampling
4: procedure TRAINEPINN
5:   Use a pre-trained base PINN with fixed parameters  $\xi$ 
6:   Initialize epinet learnable parameters  $\eta^L$  and fix the prior network weights ( $\eta^P$ , not trained)
7:   repeat
8:     Sample collocation points, boundary points, and (if available) data points
9:     Sample epistemic index  $z \sim P_z$  ▷ One  $z$  per minibatch
10:     $u_\xi(x) \leftarrow \text{BasePINN}(x; \xi)$ ,  $\tilde{x} \leftarrow \text{sg}([x, h_{\text{penultimate}}(x; \xi)])$  ▷ Stop gradient
11:     $e_{\eta^L}^L(\tilde{x}, z) \leftarrow \text{LearnableNetwork}(\tilde{x}, z; \eta^L)$ ,  $e^P(\tilde{x}, z) \leftarrow \text{PriorNetwork}(\tilde{x}, z)$ 
12:     $u_\theta(x, z) \leftarrow u_\xi(x) + e_{\eta^L}^L(\tilde{x}, z) + \alpha e^P(\tilde{x}, z)$ 
13:     $\mathcal{L}_{\text{pde}} \leftarrow \frac{1}{N_f} \sum_{i=1}^{N_f} |\mathcal{N}_x(u_\theta(x_i^f, z); \lambda) - \bar{f}_i|^2$ ,  $\mathcal{L}_{\text{boundary}} \leftarrow \frac{1}{N_b} \sum_{i=1}^{N_b} |\mathcal{B}_x(u_\theta(x_i^b, z); \lambda) - \bar{b}_i|^2$ 
14:     $\mathcal{L}_{\text{data}} \leftarrow \frac{1}{N_u} \sum_{i=1}^{N_u} |u_\theta(x_i^u, z) - \bar{u}_i|^2$  (if data are available)
15:    Minimize  $\mathcal{L}_{\text{total}} = \mathcal{L}_{\text{data}} + \mathcal{L}_{\text{pde}} + \mathcal{L}_{\text{boundary}}$  w.r.t.  $\eta^L$ 
16:   until convergence
17: end procedure
18: procedure ESTIMATEUNCERTAINTY( $x, M$ )
19:   For  $i = 1, \dots, M$ : sample  $z_i \sim P_z$  and set  $u_i \leftarrow u_\xi(x) + e_{\eta^L}(\tilde{x}, z_i)$ 
20:    $\mu_u(x) \leftarrow \frac{1}{M} \sum_{i=1}^M u_i$  ▷ Mean prediction
21:    $\sigma_u^2(x) \leftarrow \frac{1}{M} \sum_{i=1}^M (u_i - \mu_u(x))^2$  ▷ Variance
22:   return  $\mu_u(x), \sigma_u^2(x)$ 
23: end procedure

```

$$\mathcal{L}_{\text{data}} = \frac{1}{N_u} \sum_{i=1}^{N_u} |u_\theta(x_i^u) - \bar{u}_i|^2, \quad (12a)$$

$$\mathcal{L}_{\text{pde}} = \frac{1}{N_f} \sum_{i=1}^{N_f} |\mathcal{N}_x(u_\theta(x_i^f); \lambda) - \bar{f}_i|^2, \quad (12b)$$

$$\mathcal{L}_{\text{boundary}} = \frac{1}{N_b} \sum_{i=1}^{N_b} |\mathcal{B}_x(u_\theta(x_i^b); \lambda) - \bar{b}_i|^2. \quad (12c)$$

The weighting parameters can be adjusted manually or in a self-adaptive manner [50, 51, 52]. Unless otherwise specified, we set $w_{\text{data}} = w_{\text{pde}} = 1$. For problems with boundary conditions, w_{bc} is typically set to 10 to ensure boundary conditions are satisfied accurately.

The term $\mathcal{L}_{\text{data}}$ represents the mean squared error between the network predictions and the available data measurements, \mathcal{L}_{pde} enforces the PDE residual at the collocation points within the domain, and $\mathcal{L}_{\text{boundary}}$ ensures that the solution satisfies the prescribed boundary conditions.

For B-PINN, we use Gaussian likelihoods over the same residual channels: u -data, PDE residual $\mathcal{N}_x(u_\theta) - f$, and boundary residual $\mathcal{B}_x(u_\theta) - b$. With fixed noise levels, the negative log-likelihood recovers the weighted squared terms above up to constants. In HMC, we do not minimize this loss; we sample the posterior over weights using these likelihoods and standard Gaussian parameter priors.

For E-PINNs, the predictive mapping is $u_\theta(x, z)$, where $z \sim P_z$ is the epistemic index. We therefore minimize the expected composite loss over z ,

$$\mathcal{L}_{\text{total}}(\theta) = \mathbb{E}_{z \sim P_z} \left[w_{\text{data}} \mathcal{L}_{\text{data}}(u_\theta(\cdot, z)) + w_{\text{pde}} \mathcal{L}_{\text{pde}}(u_\theta(\cdot, z)) + w_{\text{bc}} \mathcal{L}_{\text{boundary}}(u_\theta(\cdot, z)) \right], \quad (13)$$

approximated in practice by sampling one z per minibatch. In the present work our quantity of interest is the latent, noise-free field $u(x)$. We report epistemic uncertainty as the variance estimated by Monte Carlo sampling over z ,

$$\sigma_u^2(x) = \text{Var}_Z[u_\theta(x, Z)]. \quad (14)$$

The network parameters θ are optimized by solving the minimization problem:

$$\theta^* = \arg \min_{\theta} \mathcal{L}_{\text{total}}(\theta). \quad (15)$$

This minimization problem is solved approximately using the Adam optimization algorithm. All networks in this work are trained with the Adam optimizer, with learning rate 10^{-3} , exponential decay rates for the first and second moment estimates $\beta_1 = 0.9$ and $\beta_2 = 0.999$, respectively. Unless otherwise noted, the base PINN is trained for 100,000 epochs and the epinet for 10,000 epochs in a decoupled fashion; early stopping is not used.

Notation - Domain and operators: $\Omega \subset \mathbb{R}^d$, $\partial\Omega$; $\mathcal{N}_x(\cdot; \boldsymbol{\lambda})$, $\mathcal{B}_x(\cdot; \boldsymbol{\lambda})$; source $f(x)$. - Base PINN: parameters ξ ; output $u_\xi(x)$; last hidden activations $h_{\text{penultimate}}(x; \xi)$. - Features: $\tilde{x} = \text{sg}([x, h_{\text{penultimate}}(x; \xi)])$. - epinet: $e_{\eta^L}^L(\tilde{x}, z)$ (trainable), $e^P(\tilde{x}, z)$ (frozen); scale α . - E-PINN output: $u_\theta(x, z) = u_\xi(x) + e_{\eta^L}^L(\tilde{x}, z) + \alpha e^P(\tilde{x}, z)$, with $\theta = (\xi, \eta^L)$. - Epistemic index: $z \sim \mathcal{N}(0, I_{d_z})$, default $d_z = 8$. - Physics operators on network: $\mathcal{N}_x(u_\theta(x); \boldsymbol{\lambda})$, $\mathcal{B}_x(u_\theta(x); \boldsymbol{\lambda})$; optional residual shorthands $r_\theta(x) = \mathcal{N}_x(u_\theta(x); \boldsymbol{\lambda}) - f(x)$ and $g_\theta(x) = \mathcal{B}_x(u_\theta(x); \boldsymbol{\lambda}) - b(x)$. - Loss weights: w_{data} , w_{pde} , w_{bc} (defaults $w_{\text{data}} = w_{\text{pde}} = 1$, $w_{\text{bc}} = 10$). - Uncertainty: $\mu_u(x) = \mathbb{E}_Z[u_\theta(x, Z)]$, $\sigma_u^2(x) = \text{Var}_Z[u_\theta(x, Z)]$.

Implementation details (common across experiments): residuals and required derivatives are computed with reverse-mode automatic differentiation (PyTorch autograd). Dropout-PINNs apply dropout to all hidden layers after the activation; input and output layers have no dropout; the dropout rate p is shared across hidden layers. Inputs and outputs are left unnormalized unless explicitly stated. We enforce boundary conditions softly via $\mathcal{L}_{\text{boundary}}$ with weight $w_{\text{bc}} = 10$ unless stated otherwise. For reproducibility, experiments use fixed random seeds recorded in the code.

3 Results

We compare the three uncertainty quantification methods introduced in Section 2. The goal is to illustrate the applicability of E-PINNs for estimating epistemic uncertainty, to evaluate computational costs, and to characterize uncertainty bands.

3.1 Evaluation Metrics

We evaluate two standard metrics: *sharpness* and *coverage*. Sharpness refers to the width of predictive intervals, while coverage indicates how often these intervals contain the true values [53, 54]. As noted by [54], prediction intervals should ideally be narrow while still capturing the expected proportion of observations.

We quantify *sharpness* as the average width of the $\pm 2\sigma$ predictive intervals [53]:

$$\mu_{2\sigma}^w = \frac{4}{N} \sum_{i=1}^N \sqrt{\sigma_u^2(x_i)}, \quad (16)$$

where N denotes the number of points at which the epistemic variance $\sigma_u^2(x_i)$ is evaluated. Smaller values of $\mu_{2\sigma}^w$ indicate sharper uncertainty estimates.

In addition to sharpness, we evaluate the quality of uncertainty estimates using *empirical coverage*, which measures the percentage of true values that fall within the predicted uncertainty bounds [55]. Specifically, for a given confidence level γ (typically 95% corresponding to $\pm 2\sigma$ bounds), the empirical coverage is calculated as:

$$C_\gamma = \frac{1}{N} \sum_{i=1}^N \mathbf{1}\{|u(x_i) - \mu_u(x_i)| \leq \Phi^{-1}(\frac{1+\gamma}{2}) \sqrt{\sigma_u^2(x_i)}\}, \quad (17)$$

where $\mathbf{1}\{\cdot\}$ is the indicator function, $u(x_i)$ is the true (exact) value, $\mu_u(x_i)$ and $\sigma_u^2(x_i)$ are the predicted mean and epistemic variance at point x_i , and $\Phi^{-1}((1+\gamma)/2)$ is the appropriate quantile of the standard normal distribution (approximately 1.96 for $\gamma = 0.95$). An ideal uncertainty quantification method should achieve an empirical coverage close to the specified confidence level: a value too low indicates overconfidence, while too high suggests overly conservative models [55].

We also report the root-mean-square error (RMSE) computed with the predictive mean $\mu_u(x)$ against the exact solution on dense validation grids.

3.2 Benchmarks and Computational Setup

To ensure a fair comparison of these metrics across methods, we implement the three uncertainty quantification approaches with consistent settings. We focus exclusively on epistemic uncertainty: all reported variances arise from either sampling the HMC posterior (B-PINN), Monte Carlo dropout (Dropout-PINN), or sampling the epistemic index z (E-PINN). In physics-only settings, losses use deterministic PDE residuals with known $f(x)$ and exact boundary values; no interior u measurements are used. In data-augmented settings, we add noisy interior u observations with zero-mean Gaussian noise of standard deviation $\sigma = \rho \|u\|_\infty$, where $\|u\|_\infty$ denotes the sup norm on the evaluation domain and $\rho \in \{0.10, 0.30\}$. Equivalently, we can view this as a homoscedastic model with $\sigma_i^u \equiv \sigma$ for all i , whereas the indexed form σ_i^u would allow known heteroscedastic noise if desired.

All experiments were executed on a system with an AMD EPYC 7502 CPU. Each job ran independently using 4 CPU cores, and no GPU acceleration was used. The "Time (s)" columns in the tables report wall-clock elapsed time as follows: E-PINN totals base and epinet training time, Dropout-PINN sums training and Monte Carlo inference time, and B-PINN reports Hamiltonian Monte Carlo sampling plus inference time.

Note on uncertainty plots Within each multi-panel figure in Section 3, the vertical axis (scale) for uncertainty plots is fixed across methods. This can make E-PINN bands appear visually narrower relative to the other methods. For quantitative comparisons, refer to the tables reporting sharpness and coverage. The ablation study (Section 3.5) shows that the E-PINN standard deviation varies systematically with the noise level and other hyperparameters, indicating that E-PINN does not underestimate uncertainty under the tested settings.

For the B-PINN results (evaluated only in data-augmented regimes), we use Hamiltonian Monte Carlo with an identity mass matrix. Unless otherwise noted, the HMC parameters are: step size 5×10^{-5} , $L = 50$ leapfrog steps, 1,000 burn-in steps, and $M = 11,000$ total samples. For the 2D nonlinear Poisson case, to enhance stability, we use a smaller step size 1×10^{-5} with the same L , burn-in, and total samples. We place standard zero-mean Gaussian priors on weights and biases (e.g., $W \sim \mathcal{N}(0, 1)$, $b \sim \mathcal{N}(0, 1)$) and tune the step size to achieve the stated acceptance. In B-PINN runs we enforce boundary and physics residual channels with small noise tolerances (0.01) for HMC stability; in physics-only settings we do not evaluate B-PINN.

Boundary condition targets are generated without added noise. In B-PINN likelihoods we assign a small residual noise level to the physics and boundary channels (standard deviation 0.01) for HMC stability; optimization-based methods (Dropout-PINN and E-PINN) use squared residual losses without injected noise on these channels. For Dropout-PINNs, the same dropout rate is used during training and inference. Uncertainty bands are computed from $M = 10,000$ stochastic forward passes. For E-PINNs, we adopt a decoupled setup in which a pre-trained PINN provides features to an epinet that is trained subsequently. Unless otherwise specified, the base PINN uses three hidden layers with 32 neurons each (32, 32, 32), the epinet uses three hidden layers with 32 neurons each (32, 32, 32) and an epistemic index of dimension $d_z = 8$, and the prior network contribution is scaled by the hyperparameter α .

3.3 Forward problems

3.3.1 1D Poisson equation

In this first case we consider the 1D Poisson equation, given by

$$\lambda \frac{\partial^2 u}{\partial x^2} = f(x), \quad x \in [-1, 1], \quad (18)$$

with exact solution

$$u(x) = \sin^3(6x). \quad (19)$$

The analytical form for f follows by substituting Eq. 19 into Eq. 18. The base PINN is trained using 100 uniformly spaced collocation points in $x \in [-1, 1]$ together with exact Dirichlet boundary conditions at the endpoints. We consider Dropout-PINN (Monte Carlo dropout) and E-PINN (epinet on a pre-trained PINN) in the physics-only setting, and additionally include B-PINN (HMC posterior over weights) for the cases with noise fractions 0.10 and 0.30.

Two training regimes are examined. In a physics-only regime, models are fitted solely to the PDE residual together with the exact boundary conditions; no interior observations are used. In this setting, the reported uncertainty is epistemic, reflecting the model's uncertainty over the interior induced by the absence of interior data. In a data-augmented regime, the physics loss is complemented with 32 interior observations of $u(x)$ corrupted with Gaussian noise at relative amplitudes 0.10 and 0.30 of $\|u\|_\infty$. Across both regimes, we report sharpness (mean width of the $\pm 2\sigma$ band), empirical 95% coverage, and RMSE on u evaluated on a dense validation grid. We set the diffusion coefficient to $\lambda = 0.01$,

$N_{\text{colloc}} = 100$, $N_{\text{sensors}} = 32$, boundary-loss weight $w_{\text{bc}} = 10$, and evaluate uncertainty with $M = 10,000$ Monte Carlo samples.

We instantiate the base PINN as an MLP with three hidden layers of 32 neurons each (32, 32, 32). The epinet also uses three hidden layers with 32 neurons each (32, 32, 32), an epistemic index dimension $d_z = 8$, and a fixed prior network with hidden widths (5, 5) scaled by the factor α . In the experiments, we set $\alpha = 0.05$. For Dropout-PINNs we report results for dropout rates $p \in \{0.05, 0.10\}$.

In the physics-only setting (Fig. 2) the methods recover the overall profile, with the largest uncertainty in the interior where no data are provided. E-PINN yields comparatively narrow bands and the lowest error; Dropout-PINN produces substantially wider intervals that depend on the dropout rate (5% narrower, 10% broader).

With noisy interior observations (Fig. 3), uncertainty bands widen and mean accuracy degrades across methods. At $\rho \in \{0.10, 0.30\}$, E-PINN remains sharper and attains the smallest errors in these runs. Dropout-PINN is widest in all cases with full coverage. In these B-PINN runs, coverage equals 1.00 while bands are much wider than E-PINN and errors are larger; total runtime is higher due to HMC sampling.

In Table 1, physics-only ($\rho = 0$) shows E-PINN with narrow bands (sharpness $\mu_{2\sigma}^w \approx 0.33$) and the smallest RMSE ($\approx 7.4 \times 10^{-3}$) with coverage equal to 1.00. Dropout-PINN yields much wider intervals (about 3.31 to 4.72) and larger RMSE. B-PINN is not evaluated in this regime. With interior u data at $\rho = 0.10$ and $\rho = 0.30$, E-PINN remains sharper (about 0.23 and 0.34) and more accurate (RMSE about 3.4×10^{-2} and 9.0×10^{-2}) than B-PINN (about 0.97 and 1.84; RMSE about 0.0996 and 0.1638) while requiring less time (about 5.3×10^2 to 7.2×10^2 s vs about 1.7×10^3 s). In all settings Dropout-PINN produces the widest intervals and larger RMSE than E-PINN; in the data-augmented cases, Dropout-PINN RMSE is comparable to or slightly below B-PINN. The last column reports the E-PINN epinet-only training time (about 114 to 168 s), which applies when a base PINN is already trained.

At $\rho \in \{0.10, 0.30\}$, E-PINN remains sharper than the alternatives and attains the smallest errors in these runs. B-PINN coverage equals 1.00 in these cases with wider bands and larger RMSE than E-PINN; Dropout-PINN produces the widest intervals with full coverage.

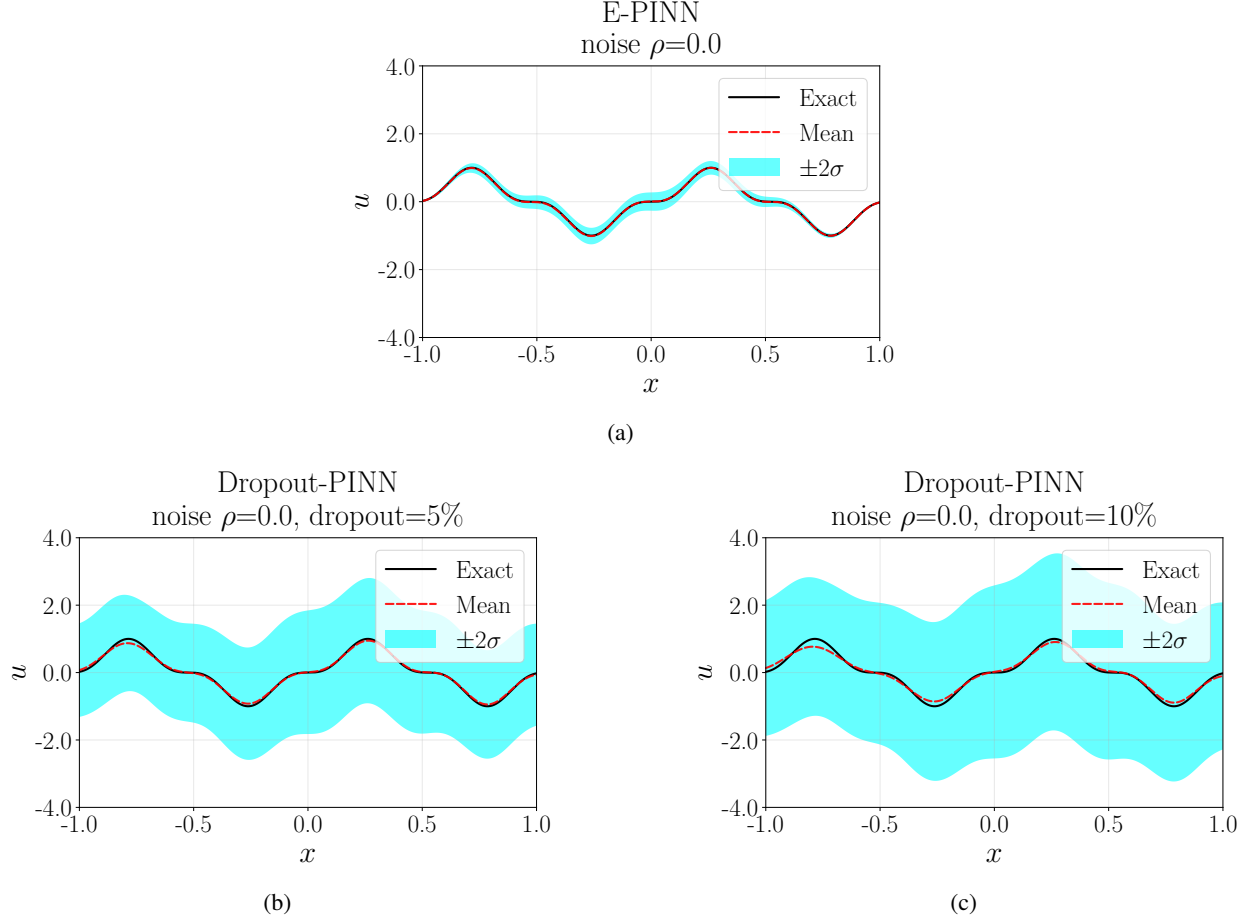


Figure 2: Mean and uncertainty predictions for u in the 1D Poisson equation (physics-only) using (a) E-PINN (top row) and (b,c) Dropout-PINN (bottom row; 5% and 10%).

Table 1: 1D Poisson: metrics vs. noise scale ρ (standard deviation $\sigma = \rho \|u\|_\infty$). RMSE is computed with the predictive mean μ_u . Time (s) is total wall-clock time; Time (epinet) (s) reports the E-PINN epinet-only training time (only populated for E-PINN rows). For $\rho = 0$ (physics-only), B-PINN is not evaluated. Lower is better for sharpness, RMSE, and time; higher is better for coverage.

ρ	Method	Sharpness $\mu_{2\sigma}^w$	Coverage (95%)	RMSE	Time (s)	Time (epinet) (s)
0.00	E-PINN	0.33	1.00	0.0074	510.75	113.83
0.00	Dropout 5%	3.31	1.00	0.0443	420.34	—
0.00	Dropout 10%	4.72	1.00	0.0830	306.02	—
0.10	E-PINN	0.23	1.00	0.0337	526.85	129.19
0.10	B-PINN	0.97	1.00	0.0996	1672.45	—
0.10	Dropout 5%	3.00	1.00	0.0700	537.27	—
0.10	Dropout 10%	4.37	1.00	0.0993	452.17	—
0.30	E-PINN	0.34	1.00	0.0901	715.71	168.11
0.30	B-PINN	1.84	1.00	0.1638	1670.35	—
0.30	Dropout 5%	2.55	1.00	0.1576	366.70	—
0.30	Dropout 10%	3.69	1.00	0.1611	431.00	—

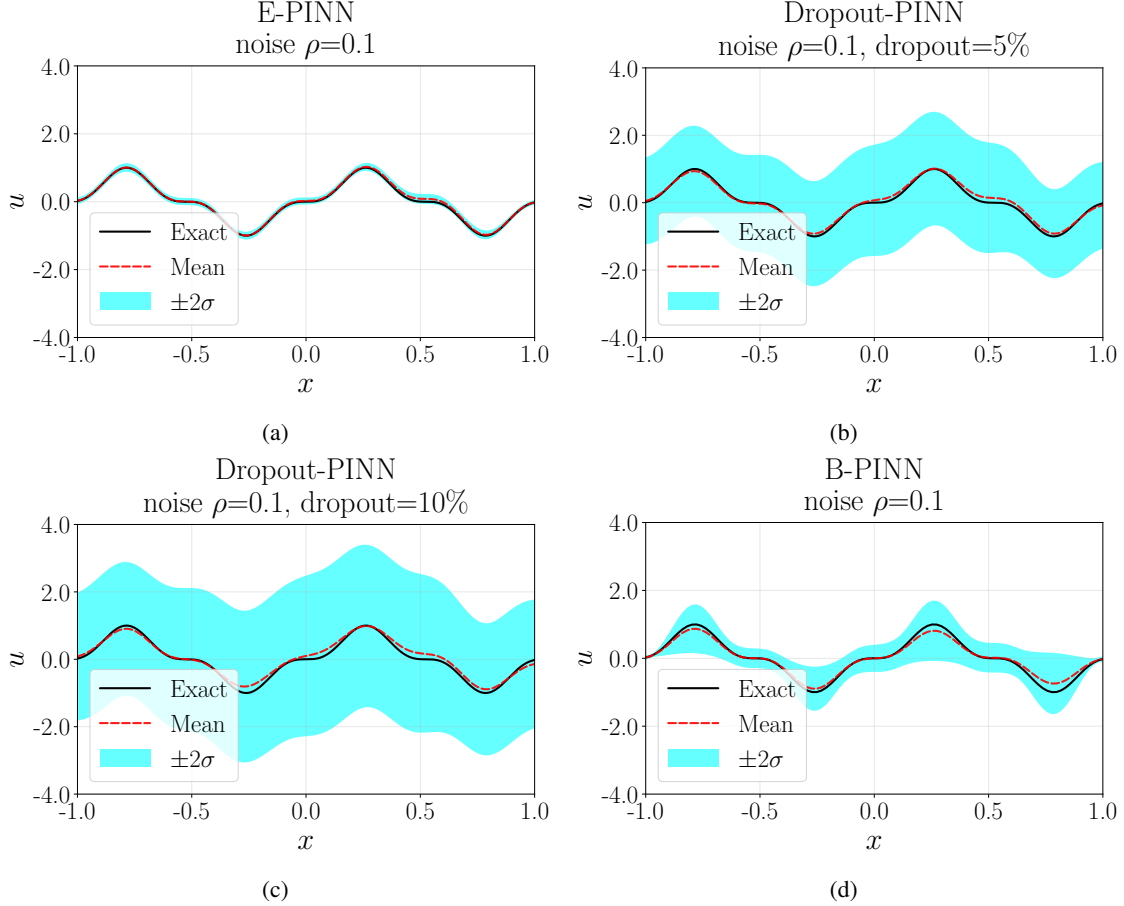


Figure 3: Mean and uncertainty predictions for u in the 1D Poisson equation (physics + interior data, Gaussian noise with $\sigma = 0.10 \|u\|_\infty$) using (a) E-PINN (b) Dropout-PINN (5%) (c) Dropout-PINN (10%) (d) B-PINN.

3.3.2 1D nonlinear Poisson equation

In this section we consider the 1D nonlinear Poisson equation, given by,

$$\lambda \frac{\partial^2 u}{\partial x^2} + k \tanh(u) = f(x), \quad x \in [-0.7, 0.7], \quad (20)$$

with exact solution given by,

$$u(x) = \sin^3(6x), \quad (21)$$

with constants $\lambda = 0.01$ and $k = 0.7$. The analytical form for f can be computed by substituting Eq. 21 into Eq. 20. The base PINN is trained using 100 collocation points uniformly distributed in $x \in [-0.7, 0.7]$ with exact boundary conditions at the endpoints. We evaluate two scenarios: (i) physics-only (no interior data) and (ii) physics + noisy u data with 32 interior sensors (fractions 0.10 and 0.30 of $\|u\|_\infty$). We do not add noise to the PDE residual or boundary values in either case. The epinet prior scaling is set to $\alpha = 0.05$.

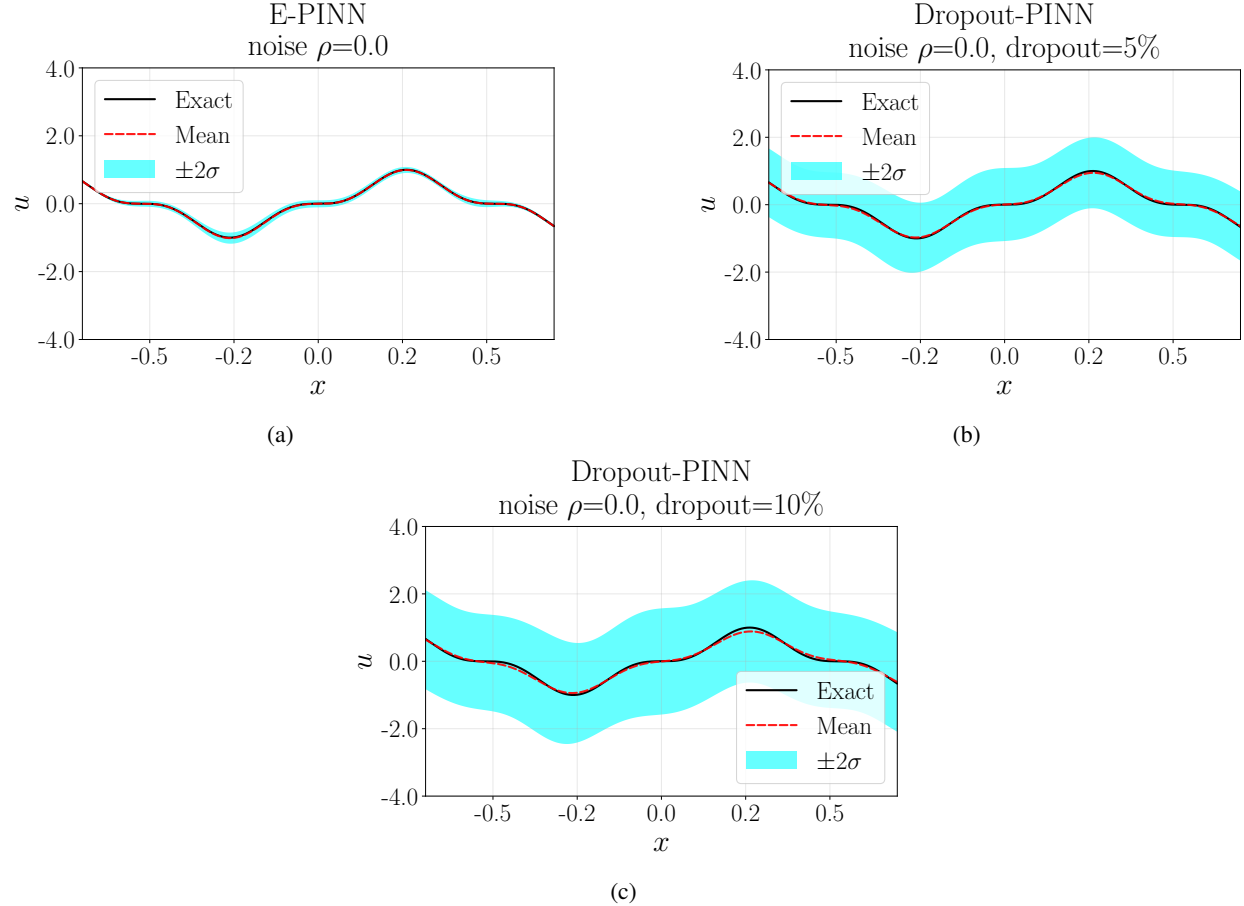


Figure 4: Mean and uncertainty predictions for u in 1D nonlinear Poisson (physics-only, no interior data) using (a) E-PINN (b) Dropout-PINN (5%) (c) Dropout-PINN (10%). B-PINN is not evaluated in physics-only.

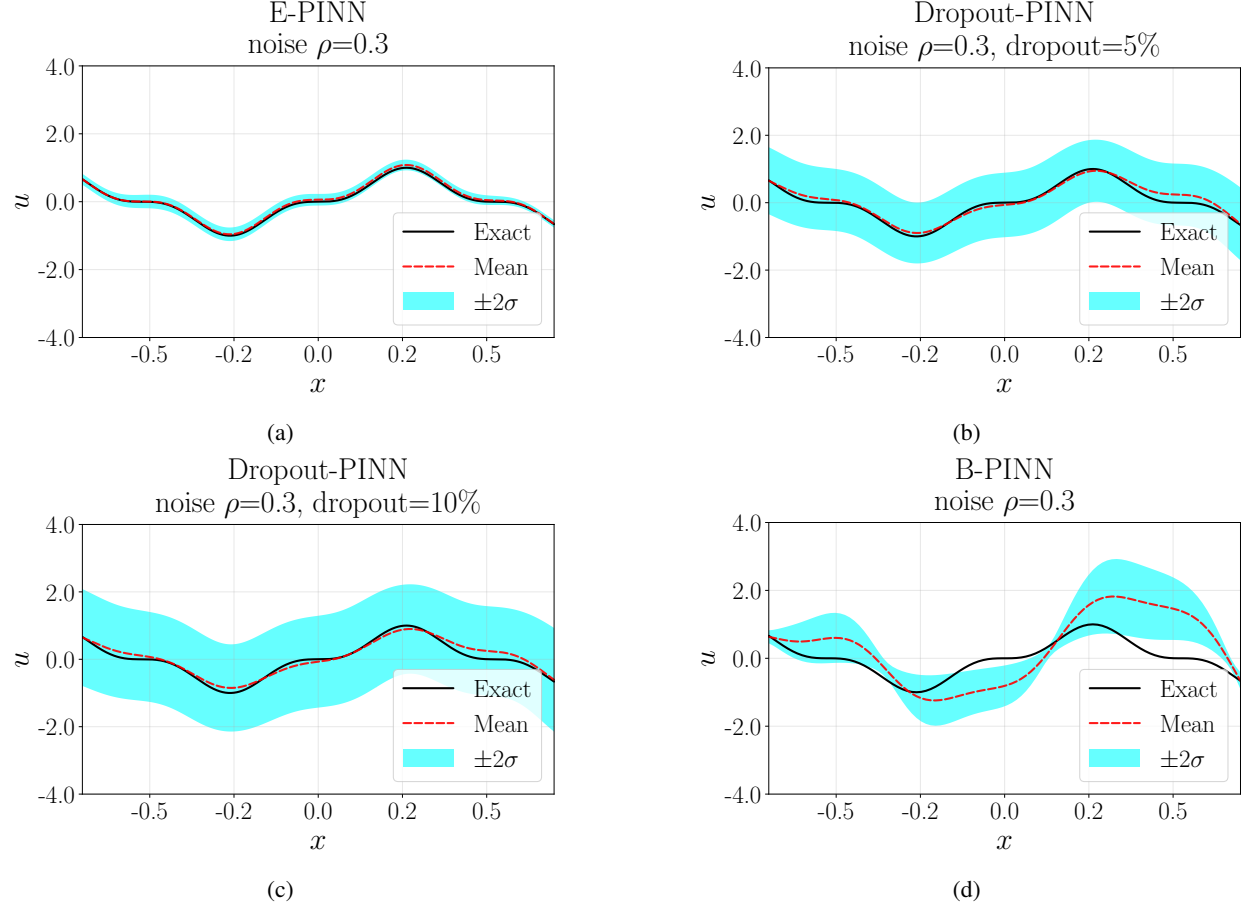


Figure 5: Mean and uncertainty predictions for u in 1D nonlinear Poisson (Gaussian noise, $\sigma = 0.30 \|u\|_\infty$) using (a) E-PINN (b) Dropout-PINN (5%) (c) Dropout-PINN (10%) (d) B-PINN.

Table 2: 1D nonlinear Poisson: metrics vs. noise scale ρ (standard deviation $\sigma = \rho \|u\|_\infty$). RMSE is computed with the predictive mean μ_u . Time (s) is total wall-clock time; Time (epinet) (s) reports the E-PINN epinet-only training time (only populated for E-PINN rows). For $\rho = 0$ (physics-only), B-PINN is not evaluated. (Sharpness/time/RMSE: lower is better; coverage: higher is better.)

ρ	Method	Sharpness $\mu_{2\sigma}^w$	Coverage (95%)	RMSE	Time (s)	Time (epinet) (s)
0.00	E-PINN	0.20	1.00	0.0065	601.96	128.14
0.00	Dropout 5%	2.05	1.00	0.0256	391.66	—
0.00	Dropout 10%	2.97	1.00	0.0516	387.82	—
0.10	E-PINN	0.16	1.00	0.0123	611.54	141.42
0.10	B-PINN	0.61	1.00	0.0314	1719.08	—
0.10	Dropout 5%	2.07	1.00	0.0416	400.50	—
0.10	Dropout 10%	2.96	1.00	0.0644	557.71	—
0.30	E-PINN	0.34	1.00	0.0494	552.38	132.48
0.30	B-PINN	1.26	0.51	0.7618	1763.16	—
0.30	Dropout 5%	1.90	1.00	0.1110	500.60	—
0.30	Dropout 10%	2.72	1.00	0.1196	369.77	—

Across these regimes (Table 2), in the physics-only setting E-PINN yields calibrated, narrow bands ($\mu_{2\sigma}^w \approx 0.20$) with the smallest error (RMSE $\approx 6.5 \times 10^{-3}$). With interior u data at $\rho = 0.10$ and $\rho = 0.30$, E-PINN remains sharp with full coverage and lower RMSE than the alternatives. Dropout-PINN produces substantially wider intervals (about 1.9 to

3.0) and larger errors across noise levels. In the B-PINN runs, coverage equals 1.00 at $\rho = 0.10$ with moderate error ($\text{RMSE} \approx 3.1 \times 10^{-2}$), while at $\rho = 0.30$ coverage drops (≈ 0.51) and RMSE increases ($\approx 7.6 \times 10^{-1}$). This failure at $\rho = 0.30$ reflects posterior pathologies under the fixed HMC configuration on a stiff, nonlinear residual: under-dispersion and poor exploration yield under-coverage and a biased mean. Smaller step sizes, better preconditioning (e.g., mass adaptation), or more samples could alleviate this at the cost of higher computational cost. The last column reports the E-PINN epinet-only training time, the incremental cost when a base PINN is already trained.

3.3.3 1D flow through a porous medium

We consider steady flow through a horizontal channel filled with a uniform porous medium. Let $x \in [0, 1]$ denote the wall-normal coordinate and $u(x)$ the streamwise velocity. The dynamics are governed by the Darcy-Brinkman equation [56, 57],

$$-\frac{\nu_e}{\phi} \frac{\partial^2 u}{\partial x^2} + \frac{\nu u}{K} = f(x), \quad x \in [0, 1], \quad (22)$$

where $(\nu_e/\phi) \partial_x^2 u$ represents effective viscous diffusion in the porous matrix, $(\nu/K) u$ is the Darcy drag, and $f(x)$ is an external body force that absorbs the streamwise pressure gradient.

The exact solution is given by [15, 56]:

$$u(x) = \frac{fK}{\nu} \left[1 - \frac{\cosh\left(r(x - \frac{H}{2})\right)}{\cosh\left(\frac{rH}{2}\right)} \right], \quad (23)$$

and

$$r = \sqrt{\frac{\nu\phi}{\nu_e K}}. \quad (24)$$

For this case, we take the effective viscosity as $\nu_e = 10^{-3}$, fluid viscosity $\nu = 10^{-3}$, porosity $\phi = 0.4$, permeability $K = 10^{-3}$, and channel height $H = 1$. We impose no-slip Dirichlet boundary conditions, $u(0) = u(1) = 0$; boundary values are treated as exact (noise-free) and are enforced via the boundary condition loss with weight $w_{bc} = 10$. The base PINN is trained using 64 collocation points uniformly distributed in $x \in [0, 1]$ with exact boundary conditions. We evaluate two scenarios: (i) physics-only (PDE + exact BC; no interior data) and (ii) physics + noisy u data at 32 interior sensors, where noise is injected on u as a fraction of $\|u\|_\infty$ (fractions 0.10 and 0.30).

Figures 6 (physics-only) and 7 ($\rho = 0.10$) illustrate the mean and uncertainty for u . In the physics-only case, E-PINN and Dropout-PINN recover the profile, including steep boundary-layer gradients, with uncertainty bands that widen away from the walls; Dropout-PINN bands grow with the dropout rate. With noisy interior sensors ($\rho = 0.10$), means degrade across methods near sharp gradients; E-PINN remains sharp, Dropout-PINN depends on the dropout rate, and B-PINN attains slightly narrower bands with higher RMSE.

Table 3 reports sharpness, coverage, RMSE, and time. In physics-only ($\rho = 0$), E-PINN attains narrow bands ($\mu_{2\sigma}^w \approx 0.132$) with full coverage and low RMSE (≈ 0.0055); Dropout-PINN is much wider (about 2.16 to 3.13) with higher RMSE (about 0.027 to 0.048). With interior u data ($\rho = 0.10$ and $\rho = 0.30$), E-PINN remains calibrated and sharp (about 0.239 and 0.182) with low RMSE (about 0.0034 and 0.013) at total times of about 4.5×10^2 to 4.8×10^2 s. B-PINN achieves slightly smaller sharpness (about 0.183 at both noise levels) but with markedly higher RMSE and higher total time. In these data-augmented runs, the B-PINN bands are narrow but centered on inaccurate means, as reflected by the high RMSE despite full coverage. Dropout-PINN produces the widest intervals with higher RMSE. The last column lists epinet-only training time for E-PINN (about 133 to 198 s), the incremental cost when reusing a trained base model.

Relative to [15], the B-PINN discrepancy arises from the noise model: their tests perturb the source and boundary measurements, while here noise is applied only to interior u sensors with no added noise on the physics and boundary channels (in B-PINN likelihoods we use a small residual noise level of 0.01 for stability). Direct noise on u leads to broader posteriors under the same PDE constraints, consistent with Table 3.

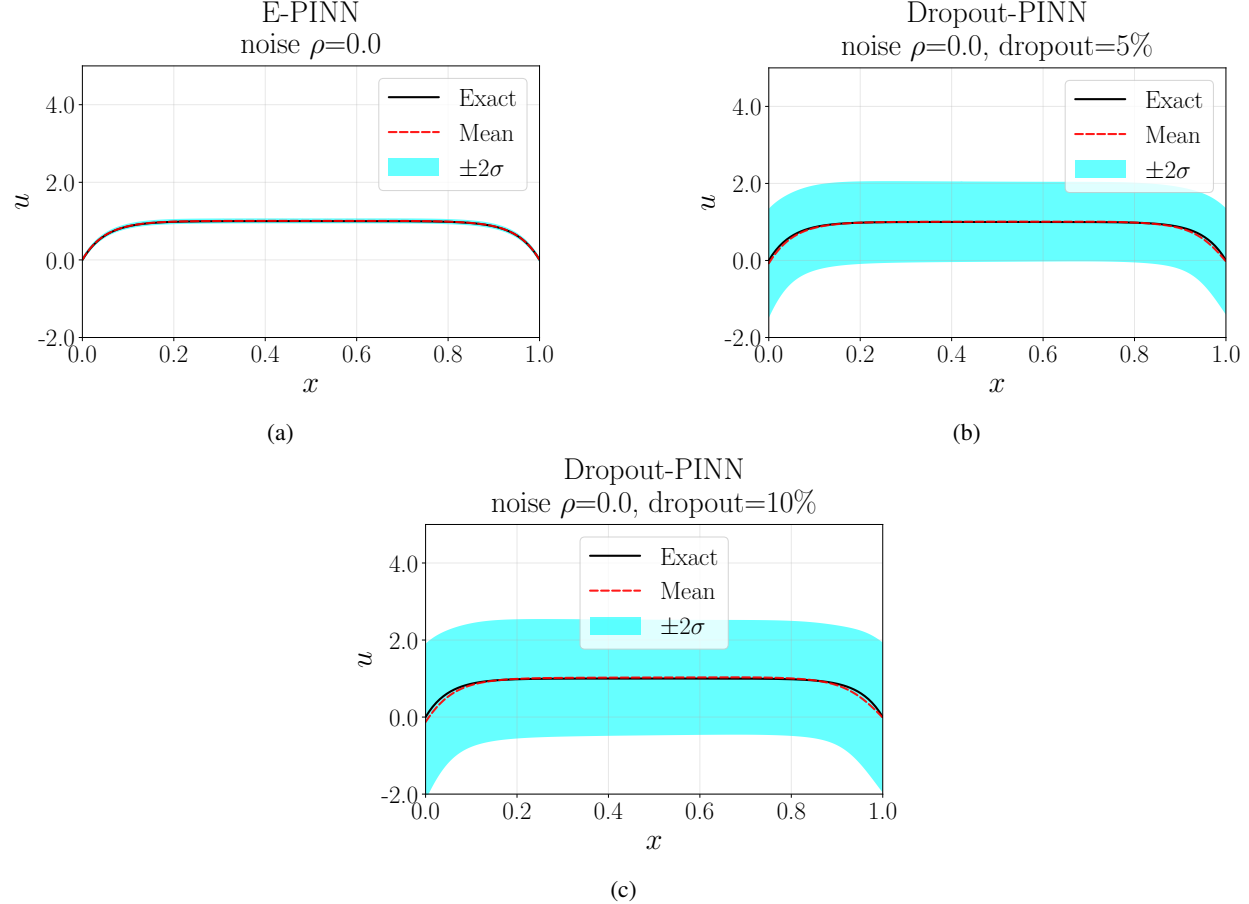


Figure 6: Mean and uncertainty predictions for u in a 1D porous medium (physics-only, no interior data) using (a) E-PINN (b) Dropout-PINN (5%) (c) Dropout-PINN (10%). B-PINN is not evaluated in physics-only.

Table 3: 1D porous medium: metrics vs. noise scale ρ (standard deviation $\sigma = \rho \|u\|_\infty$). RMSE is computed with the predictive mean μ_u . Time (s) is total wall-clock time; Time (epinet) (s) reports the E-PINN epinet-only training time (only populated for E-PINN rows). For $\rho = 0$ (physics-only), B-PINN is not evaluated. (Sharpness/time/RMSE: lower is better; coverage: higher is better.)

ρ	Method	Sharpness $\mu_{2\sigma}^w$	Coverage (95%)	RMSE	Time (s)	Time (epinet) (s)
0.00	E-PINN	0.13	1.00	0.0055	508.94	197.62
0.00	Dropout 5%	2.16	1.00	0.0275	324.76	—
0.00	Dropout 10%	3.13	1.00	0.0478	322.63	—
0.10	E-PINN	0.24	1.00	0.0034	448.23	133.26
0.10	B-PINN	0.18	1.00	0.1087	1703.46	—
0.10	Dropout 5%	2.13	1.00	0.0300	361.57	—
0.10	Dropout 10%	3.12	1.00	0.0618	460.12	—
0.30	E-PINN	0.18	1.00	0.0132	478.58	136.90
0.30	B-PINN	0.18	1.00	0.1113	1786.83	—
0.30	Dropout 5%	2.09	1.00	0.0378	350.92	—
0.30	Dropout 10%	3.05	1.00	0.0663	358.40	—

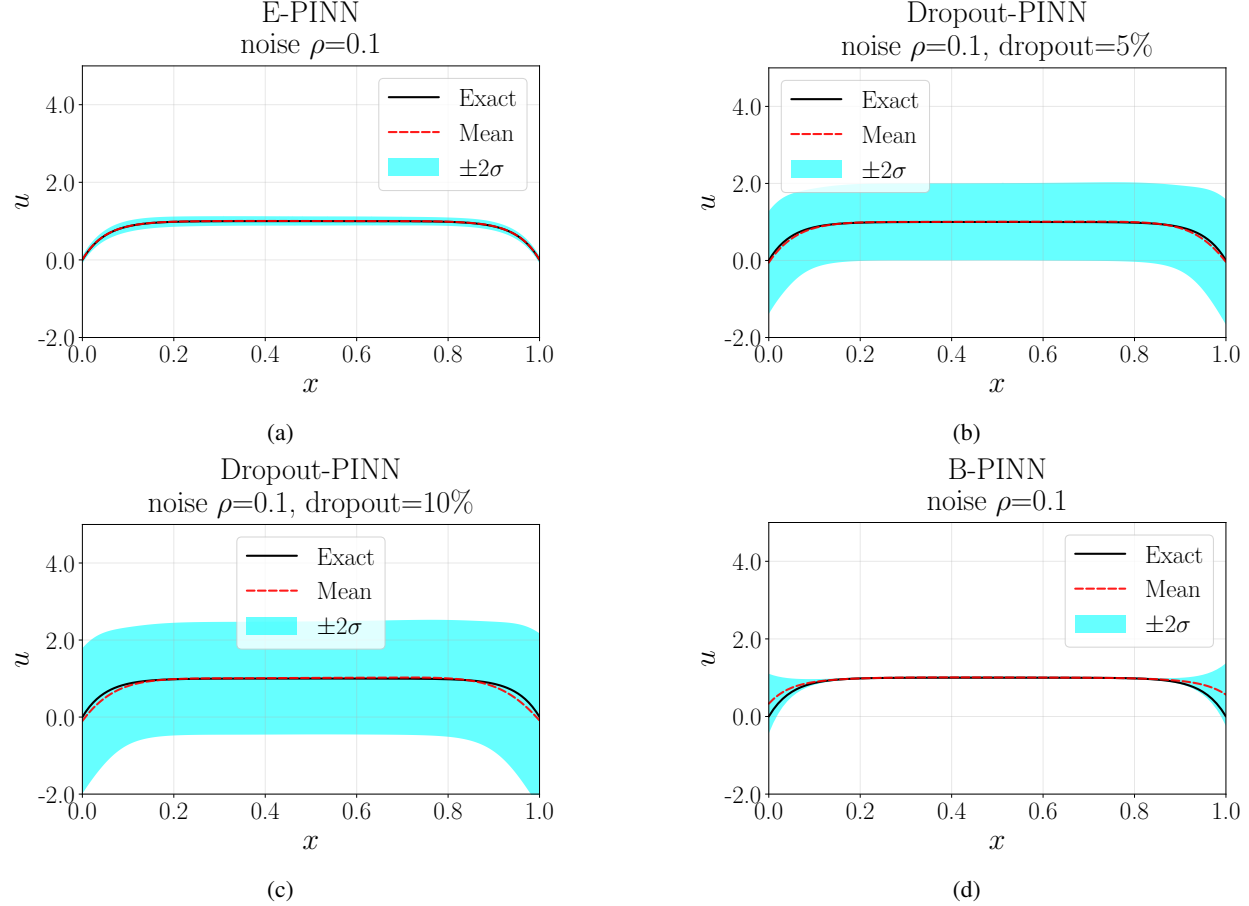


Figure 7: Mean and uncertainty predictions for u in a 1D porous medium (Gaussian noise, $\sigma = 0.10 \|u\|_\infty$) using (a) E-PINN (b) Dropout-PINN (5%) (c) Dropout-PINN (10%) (d) B-PINN.

3.3.4 2D nonlinear Poisson equation

We assess scalability beyond one dimension on a 2D nonlinear Poisson problem posed on $\Omega = [-1, 1]^2$. We set the epinet prior scaling to $\alpha = 0.05$. The governing equation is

$$\lambda \left(\frac{\partial^2 u}{\partial x^2} + \frac{\partial^2 u}{\partial y^2} \right) + u(u^2 - 1) = f(x, y), \quad (x, y) \in \Omega, \quad \lambda = 0.01, \quad (25)$$

with Dirichlet boundary conditions on $\partial\Omega$. For evaluation, we adopt the manufactured (exact) solution

$$u(x, y) = \sin(\pi x) \sin(\pi y), \quad (26)$$

and obtain $f(x, y)$ by substituting this expression into (25). In direct analogy with the 1D cases, we consider two regimes: (i) physics-only (PDE + exact boundary values; no interior data), and (ii) physics augmented with noisy interior measurements of u at a sparse set of sensors, where the noise level is a fraction of $\|u\|_\infty$ (fractions 0.10, 0.30). We report sharpness (mean width of the $\pm 2\sigma$ band), empirical 95% coverage, and RMSE on dense grids. For this case, we report B-PINN in the data-augmented setting.

Figure 8 summarizes the physics-only case (mean, standard deviation, and error); Figure 9 shows the corresponding comparison at $\rho = 0.30$. Additional plots for $\rho = 0.10$ are provided in Appendix 6.

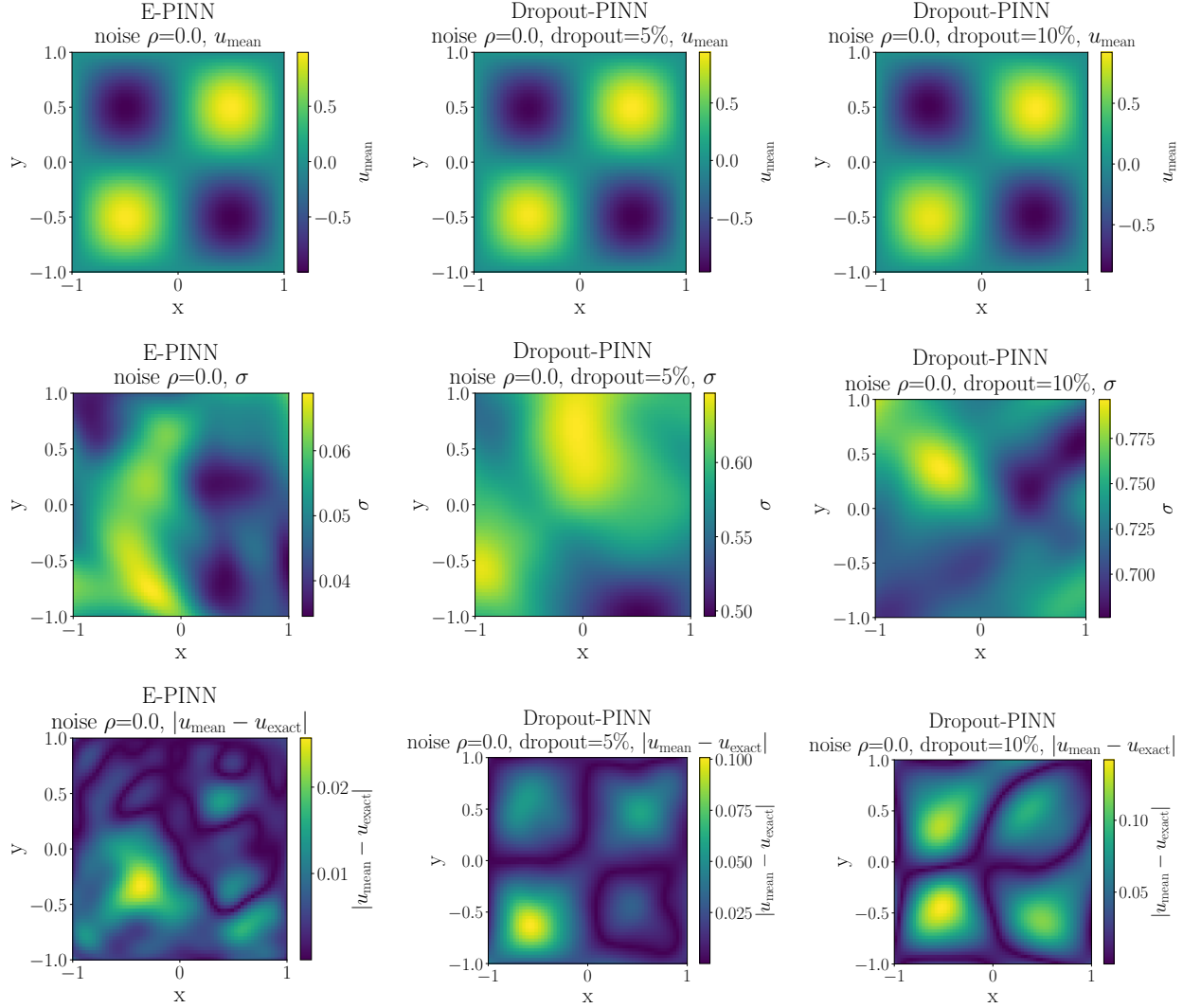


Figure 8: 2D nonlinear Poisson (physics-only): top, mean u ; middle, epistemic standard deviation; bottom, absolute error. Columns: E-PINN (left), Dropout-PINN (5%) (center), Dropout-PINN (10%) (right).

Table 4: 2D nonlinear Poisson: metrics vs. noise scale ρ (standard deviation $\sigma = \rho \|u\|_\infty$). RMSE is computed with the predictive mean μ_u . Time (s) is total wall-clock time; Time (epinet) (s) reports the E-PINN epinet-only training time (only populated for E-PINN rows). For $\rho = 0$ (physics-only), B-PINN is not evaluated. (Sharpness/time/RMSE: lower is better; coverage: higher is better.)

ρ	Method	Sharpness $\mu_{2\sigma}^w$	Coverage (95%)	RMSE	Time (s)	Time (epinet) (s)
0.00	E-PINN	0.20	1.00	0.0081	1698.99	478.19
0.00	Dropout 5%	2.36	1.00	0.0321	1180.79	–
0.00	Dropout 10%	2.91	1.00	0.0589	1202.74	–
0.10	E-PINN	0.33	1.00	0.0082	1699.26	493.76
0.10	B-PINN	0.26	0.99	0.0428	2623.84	–
0.10	Dropout 5%	2.08	1.00	0.0425	1298.83	–
0.10	Dropout 10%	2.62	1.00	0.0697	1333.20	–
0.30	E-PINN	0.32	1.00	0.0104	1764.36	510.09
0.30	B-PINN	0.31	0.99	0.0493	2555.59	–
0.30	Dropout 5%	2.22	1.00	0.0637	1212.97	–
0.30	Dropout 10%	3.19	1.00	0.0767	2480.38	–

Across these regimes (Table 4), E-PINN attains calibrated bands with narrow sharpness in physics-only ($\mu_{2\sigma}^w \approx 0.20$) and remains sharp with interior u data (≈ 0.33 at $\rho = 0.10$, ≈ 0.32 at $\rho = 0.30$), yielding the smallest RMSEs ($\approx 8 \times 10^{-3}$ to $\approx 1 \times 10^{-2}$). Dropout-PINN produces substantially wider intervals (≈ 2.1 to ≈ 3.2) with larger errors across noise levels. B-PINN coverage is 0.99 with sharpness comparable to E-PINN but higher RMSE ($\approx 4.3 \times 10^{-2}$ to $\approx 4.9 \times 10^{-2}$) and higher total runtime ($\approx 2.6 \times 10^3$ s on CPU). The last column reports the E-PINN epinet-only training time ($\approx 4.8 \times 10^2$ to $\approx 5.1 \times 10^2$ s), the incremental cost when a base PINN is already trained.

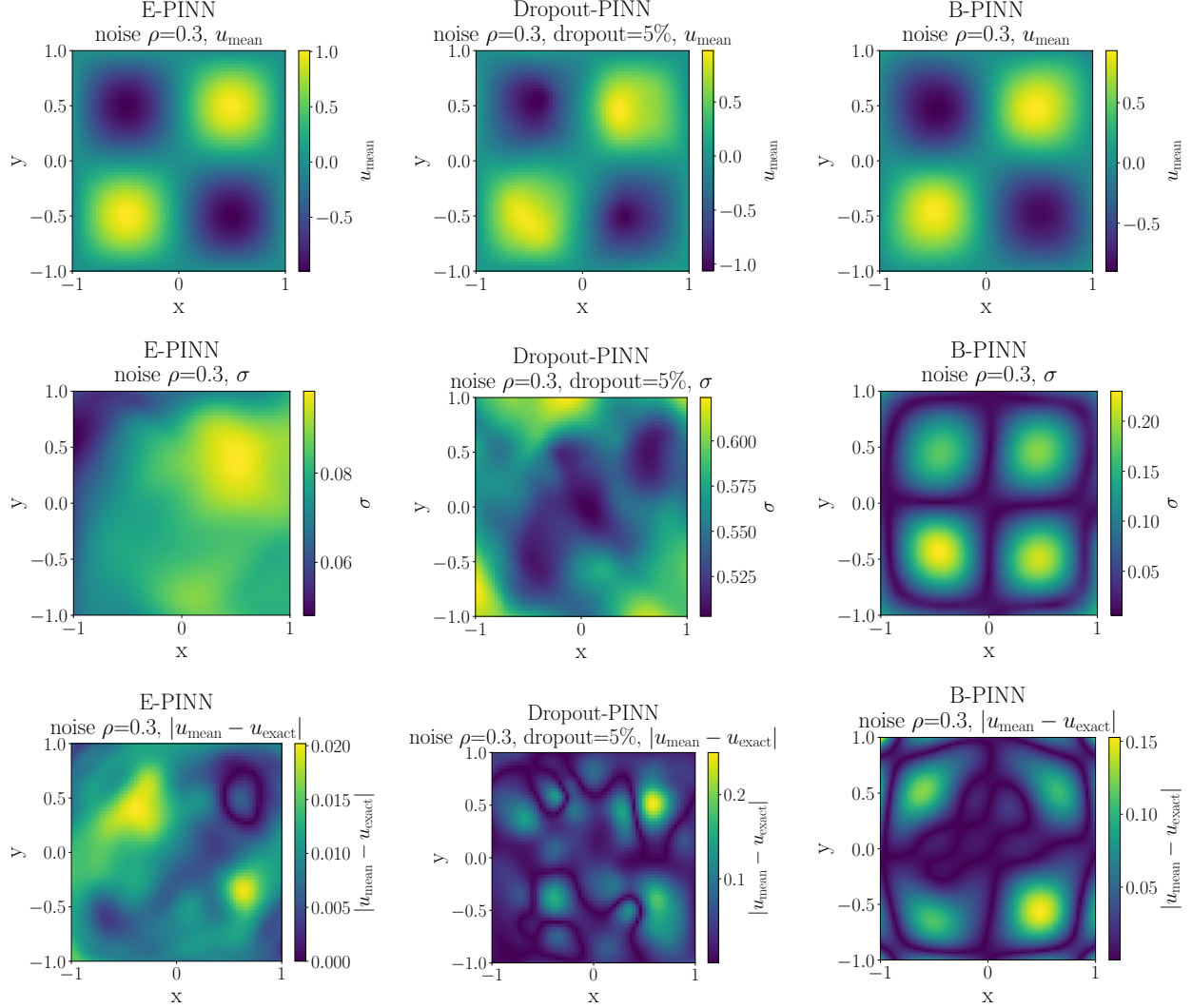


Figure 9: 2D nonlinear Poisson ($\rho = 0.30$): top, mean u ; middle, epistemic standard deviation; bottom, absolute error. Columns: E-PINN (left), Dropout-PINN (center), B-PINN (right).

3.4 Inverse problems

3.4.1 1D heat equation

We demonstrate inverse modeling by estimating the thermal diffusivity κ in the 1D heat equation with initial and boundary conditions:

$$\frac{\partial u}{\partial t} = \kappa \frac{\partial^2 u}{\partial x^2}, \quad x \in [0, 1], t \in [0, 1], \quad (27a)$$

$$u(x, 0) = \sin(\pi x), \quad (27b)$$

$$u(0, t) = 0, \quad u(1, t) = 0. \quad (27c)$$

Training uses noise-free PDE, boundary, and initial-condition targets together with noisy interior measurements of $u(x, t)$ at space-time sensors, where the noise level is a fraction of $\|u\|_\infty$ (fractions 0.10, 0.30). The data are generated with true thermal diffusivity $\kappa = 0.1$. We predict a spatiotemporal field $\hat{\kappa}(x, t)$ jointly with u and penalize its variance

so that the learned $\hat{\kappa}$ is effectively constant; we summarize κ by spatiotemporal averaging.

$$\mathcal{L}_\kappa = \text{Var}_{(x,t) \in \mathcal{C}}[\hat{\kappa}(x,t)], \quad (28)$$

$$\mathcal{L}_{\text{pde}} = \frac{1}{N_f} \sum_{i=1}^{N_f} \left| \frac{\partial u_\theta}{\partial t}(x_i^f, t_i^f) - \hat{\kappa}(x_i^f, t_i^f) \frac{\partial^2 u_\theta}{\partial x^2}(x_i^f, t_i^f) \right|^2. \quad (29)$$

The heat inverse objective augments the generic loss with \mathcal{L}_κ ; $\hat{\kappa}$ is shared across methods. Under this design, E-PINN yields a distribution over κ via Monte Carlo sampling over the epistemic index z (with epinet prior scaling $\alpha = 0.05$); Dropout-PINN yields a κ distribution via Monte Carlo dropout; and B-PINN yields a κ posterior via Hamiltonian Monte Carlo sampling of the network weights.

We summarize κ estimates and wall-clock timings across noise levels in Table 5. For visual reference, Figure 12 shows representative κ histograms for the three methods (data-augmented regime). Because this is a temporal problem, the table reports moments of the inferred scalar parameter κ from Monte Carlo/HMC samples, while the line plots elsewhere show instantaneous $u(x, t)$ means and $\pm 2\sigma$ bands at fixed times. For E-PINN, the "epinet time" column reports the incremental cost when a base PINN is already trained. At $\rho = 0.30$, the B-PINN posterior mean underestimates κ (about 0.078 versus the true 0.1), while E-PINN and Dropout-PINN remain centered near 0.1 with larger dispersion for dropout. In the B-PINN implementation used here, the likelihood includes boundary/initial-condition and PDE-residual channels with strong but finite precisions together with interior u -data; the underestimation reflects the information balance under these fixed precisions.

Table 5: Inverse heat: κ (mean \pm std) and timing across Gaussian noise scales ρ (standard deviation $\sigma = \rho \|u\|_\infty$). Time (epinet) (s) is the E-PINN epinet-only training time (only populated for E-PINN rows).

ρ	Method	κ (mean \pm std)	Time (s)	Time (epinet) (s)
0.10	E-PINN	0.099 ± 0.012	4258.50	1068.63
0.10	B-PINN	0.098 ± 0.009	5553.45	—
0.10	Dropout 5%	0.100 ± 0.058	1075.56	—
0.10	Dropout 10%	0.101 ± 0.093	1073.78	—
0.30	E-PINN	0.101 ± 0.015	4238.53	1026.48
0.30	B-PINN	0.078 ± 0.019	2583.11	—
0.30	Dropout 5%	0.101 ± 0.056	1219.62	—
0.30	Dropout 10%	0.094 ± 0.119	1570.04	—

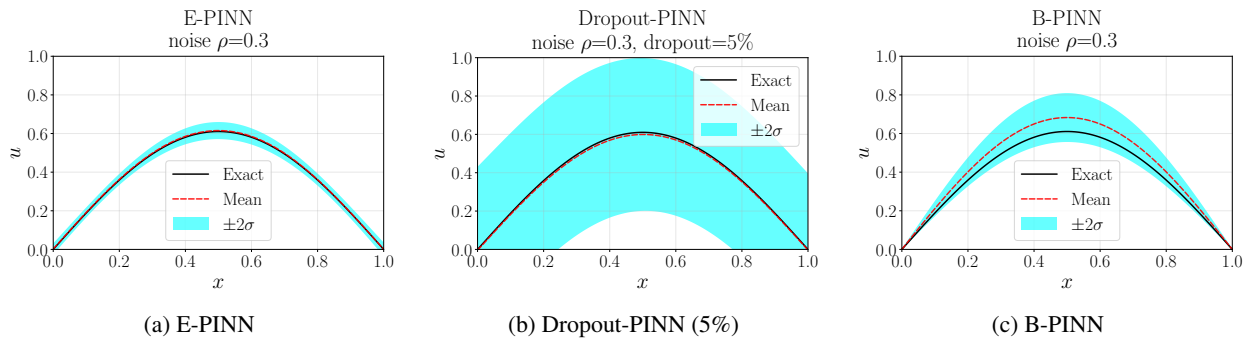


Figure 10: 1D heat equation (inverse; $\rho = 0.30$, $t = 0.50$): mean and $\pm 2\sigma$ epistemic bands for $u(x, t)$ (instantaneous slice). Methods: (a) E-PINN, (b) Dropout-PINN (5%), (c) B-PINN.

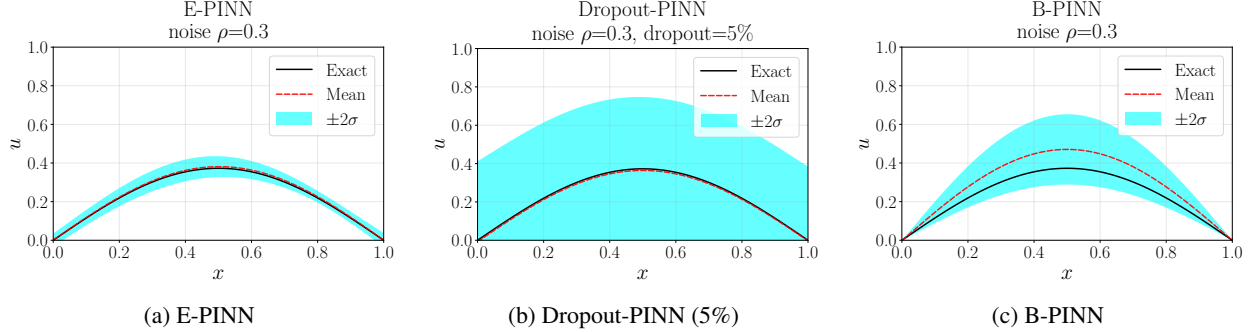


Figure 11: 1D heat equation (inverse; $\rho = 0.30$, $t = 1.00$): mean and $\pm 2\sigma$ epistemic bands for $u(x, t)$ (instantaneous slice). Methods: (a) E-PINN, (b) Dropout-PINN (5%), (c) B-PINN.

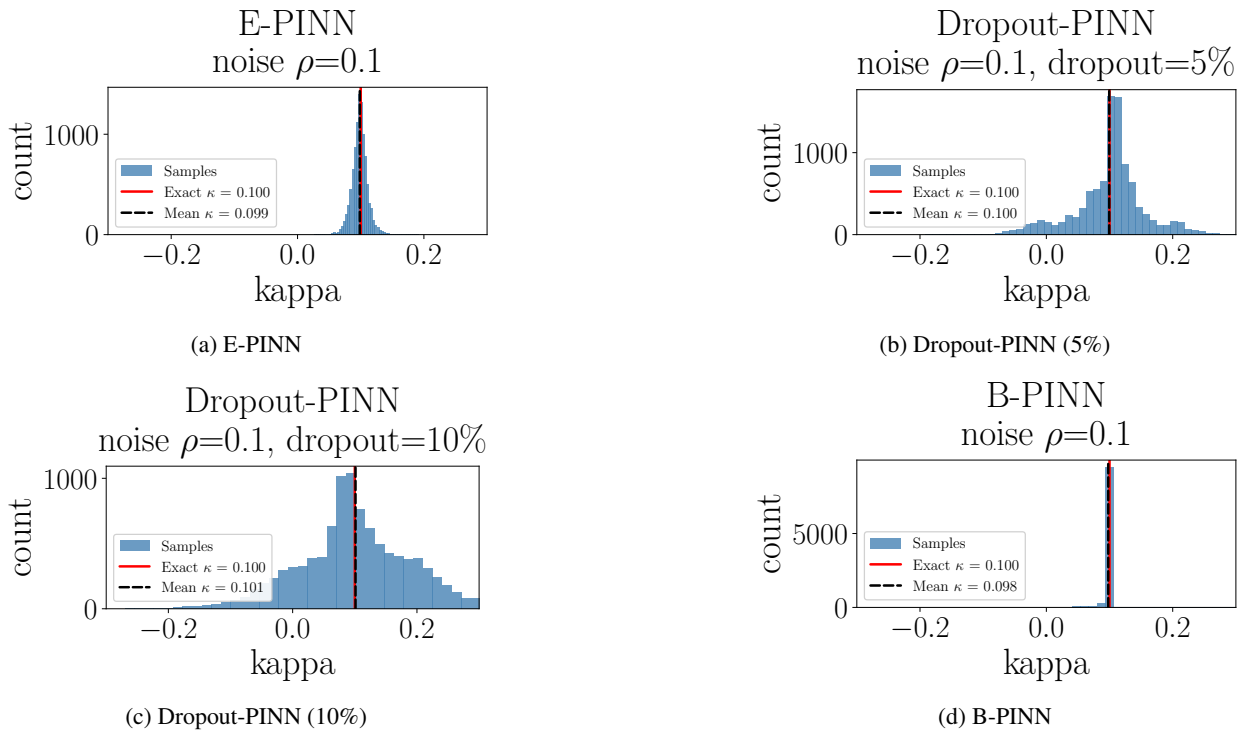


Figure 12: 1D heat equation (inverse): histograms of κ for E-PINN, Dropout-PINN (5% and 10%), and B-PINN.

3.5 Ablation study

This section studies how E-PINN hyperparameters affect mean predictions and epistemic uncertainty. All ablations use the viscous Burgers equation on $x \in [-1, 1]$, $t \in [0, 1]$,

$$\frac{\partial u}{\partial t} + u \frac{\partial u}{\partial x} - \nu \frac{\partial^2 u}{\partial x^2} = f(x, t), \quad (30)$$

with viscosity $\nu = 0.01/\pi$. We adopt the exact solution

$$u(x, t) = \sin(kx + \omega t), \quad (31)$$

with $k = \pi$ and $\omega = 2$, and set $f(x, t)$ by substituting this u into the PDE. We vary four factors: the number of collocation points N_{colloc} , the number of epinet parameters (hidden units), the epinet training epochs, and the base

network training epochs. In all ablations the base network is pre-trained and then held fixed while the epinet is trained. Unless stated otherwise, the architecture is fixed to three hidden layers of 32 units for both the base network and the epinet ((32, 32, 32)), the epistemic index has dimension $d_z = 8$, the prior contribution is scaled by $\alpha = 0.05$, the base network is trained for 10^5 epochs, and the epinet is trained for 10^4 epochs. The only quantity that changes within each ablation is the variable of interest (e.g., N_{colloc} , H , or the number of epochs).

3.5.1 Effect of number of collocation points

This section studies the effect of the number of collocation points (N_{colloc}) used for training the base network and the epinet. All runs are physics only, and architectures and training schedules are held fixed across settings. Figure 13 shows the four cases used in the study. Table 6 reports sharpness (mean width of the $\pm 2\sigma$ band), empirical 95% coverage, RMSE, and wall-clock time.

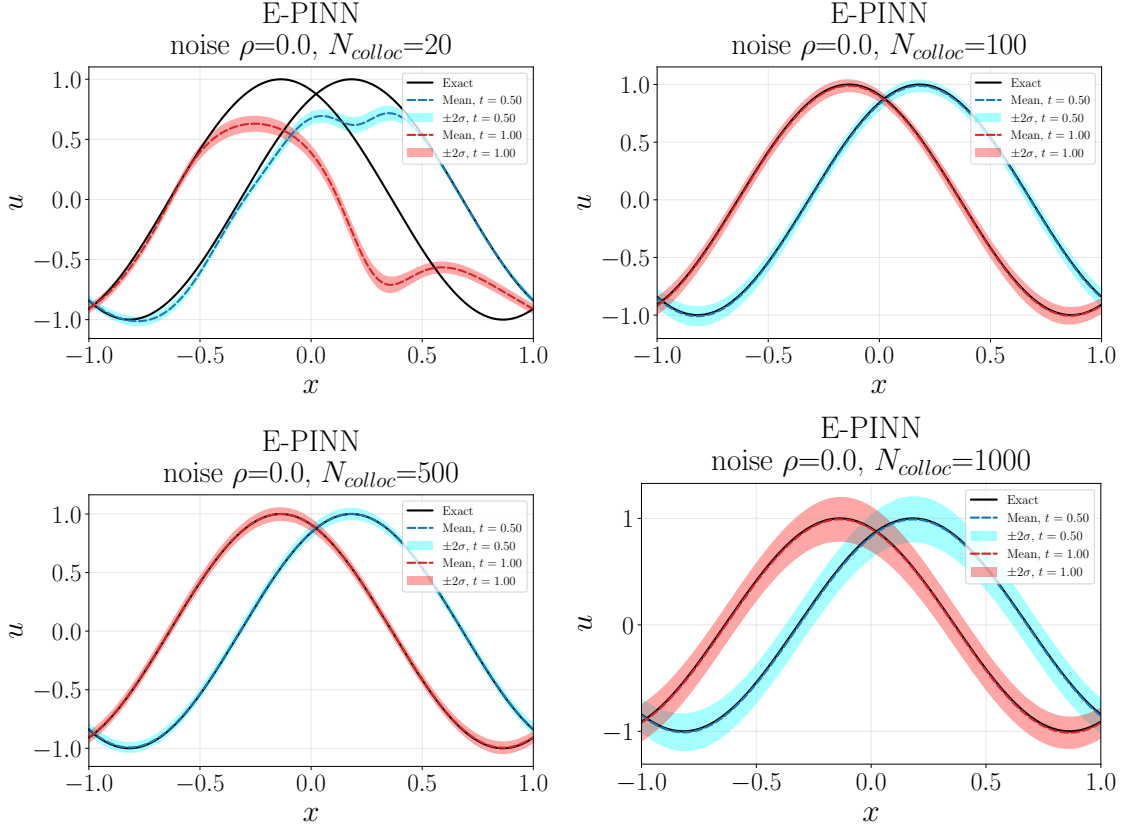


Figure 13: Effect of collocation points. Shown for $N_{\text{colloc}} \in \{20, 100, 500, 1000\}$. Each panel shows the predictive mean and $\pm 2\sigma$ epistemic bands for u ; architecture and training schedule are held fixed across runs.

Table 6: Burgers ablation (collocation): E-PINN metrics versus N_{colloc} in physics only. RMSE is computed with the predictive mean μ_u . Time (s) is total wall clock time; Time (epinet) (s) is the epinet only training time. (Sharpness/time/RMSE: lower is better; coverage: higher is better.)

N_{colloc}	Sharpness $\mu_{2\sigma}^w$	Coverage (95%)	RMSE	Time (s)	Time (epinet) (s)
20	0.09	0.35	0.2208	955.08	160.75
100	0.14	1.00	0.0101	919.99	167.39
500	0.10	1.00	0.0047	1440.84	252.71
1000	0.39	1.00	0.0118	1240.20	281.78

In this configuration (Table 6), $N_{\text{colloc}} = 20$ underfits the physics, yielding low coverage and a large error. Moving to $N_{\text{colloc}} = 100$ raises coverage to 1.00 and reduces RMSE by over an order of magnitude ($\approx 22\times$), with a slight

decrease in total time. At $N_{\text{colloc}} = 500$, sharpness narrows further and RMSE attains its minimum with higher total time. At $N_{\text{colloc}} = 1000$, the mean error increases relative to 500 and the bands widen, while time decreases relative to 500 but remains in the same range, indicating a non-monotone dependence of sharpness and error on N_{colloc} in this setup. With a fixed training budget, increasing collocation points raises residual constraint per epoch; for this PDE and optimizer schedule, $N_{\text{colloc}} \in [100, 500]$ provides a stable calibration regime where the base features remain informative for the epinet and the epinet concentrates uncertainty where the solution is most variable. At $N_{\text{colloc}} = 1000$, the base optimization is comparatively less complete under the same budget, and the epinet expresses this as wider bands while preserving nominal coverage.

3.5.2 Effect of number of epinet network parameters

This ablation varies only the epinet hidden width, H , with the number of epinet layers fixed at two. The base network architecture and all training schedules remain fixed across settings. We set $N_{\text{colloc}} = 1000$; the base network is trained for 10^5 epochs and the epinet for 10^4 epochs.

Figure 14 and Table 7 show that all settings achieve nominal coverage. For $H \in \{4, 8, 16\}$, bands are narrow ($\mu_{2\sigma}^w \approx 0.09$ to 0.16) and RMSE remains near 10^{-3} . Increasing H to 32 and 64 enlarges the bands and raises RMSE without improving coverage, with only moderate changes in time. In this setting the epinet acts as a low-variance corrector when its capacity is commensurate with the structure present in the base features; overly wide epineps increase the variance of the learned correction without improving fit to the noiseless target, which appears as wider bands and larger RMSE at similar coverage. For this problem, $H \in [8, 16]$ provides a practical trade-off across sharpness, accuracy, and time.

Table 7: Epinet width ablation: E-PINN metrics versus H . RMSE is computed with the predictive mean μ_u . Time (s) is total wall clock time; Time (epinet) (s) is the epinet only training time. (Sharpness/time/RMSE: lower is better; coverage: higher is better.)

H	Sharpness $\mu_{2\sigma}^w$	Coverage (95%)	RMSE	Time (s)	Time (epinet) (s)
4	0.09	1.00	0.0016	1172.99	237.50
8	0.12	1.00	0.0034	1210.00	248.76
16	0.16	1.00	0.0033	1186.97	246.22
32	0.37	1.00	0.0146	1194.05	254.31
64	1.09	1.00	0.0308	1320.37	299.26

3.5.3 Effect of the number of training epochs in the epinet

This ablation investigates the effect of the epinet training budget under a standardized configuration in which the architecture remains at the defaults (32, 32, 32) and $N_{\text{colloc}} = 1000$ is used for stability. We vary only the number of epinet training epochs while keeping the base network fixed at its default budget. Physics and boundary conditions are exact, and no interior u sensors are used. The epinet epochs are $\{10^4, 10^5, 10^6\}$. Figure 15 shows the three cases used in the study.

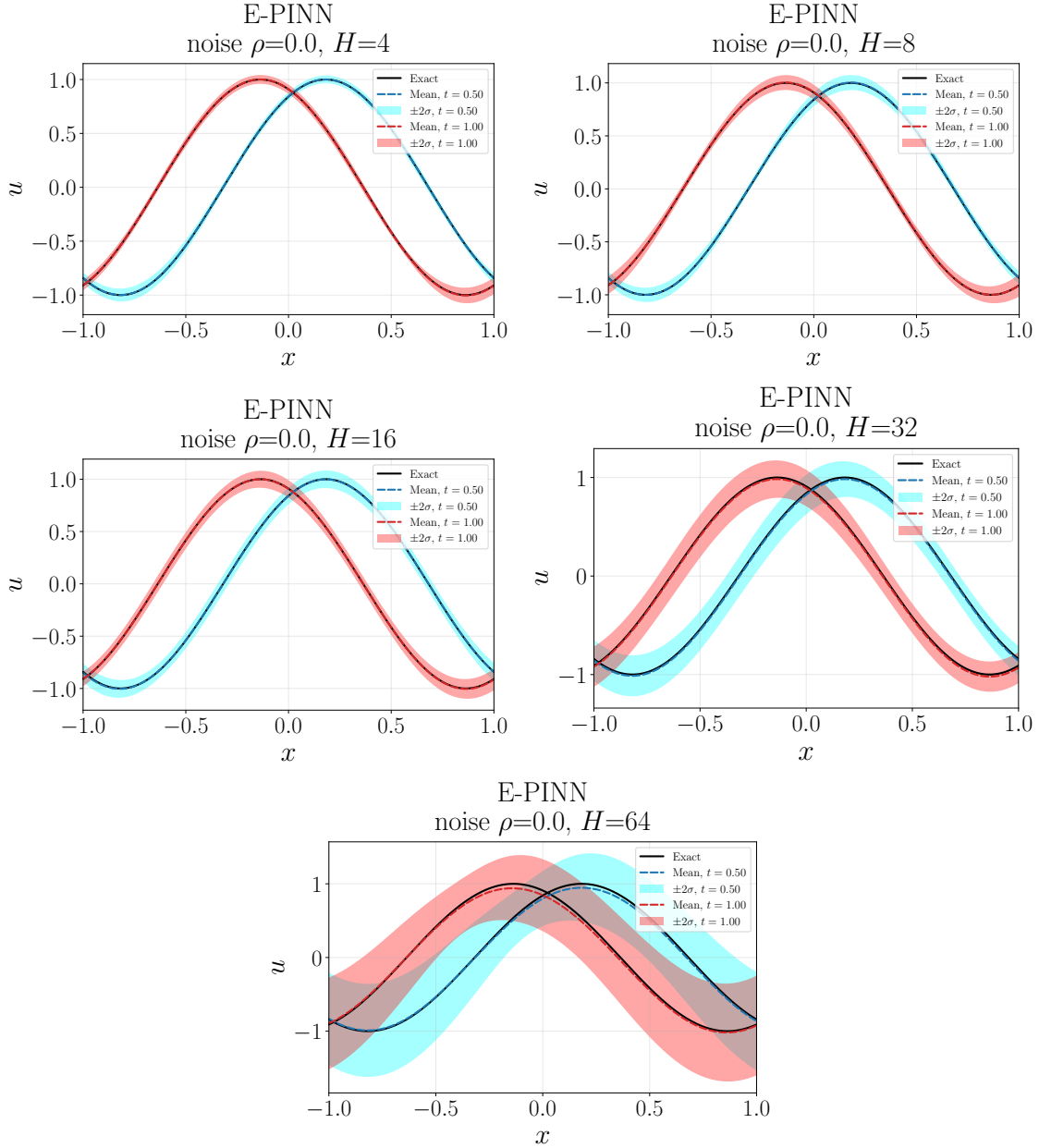


Figure 14: Effect of epinet width H . Shown for $H \in \{4, 8, 16, 32, 64\}$ with $N_{\text{colloc}} = 1000$. Each panel shows the predictive mean and $\pm 2\sigma$ epistemic bands for u ; all other settings are fixed across runs.

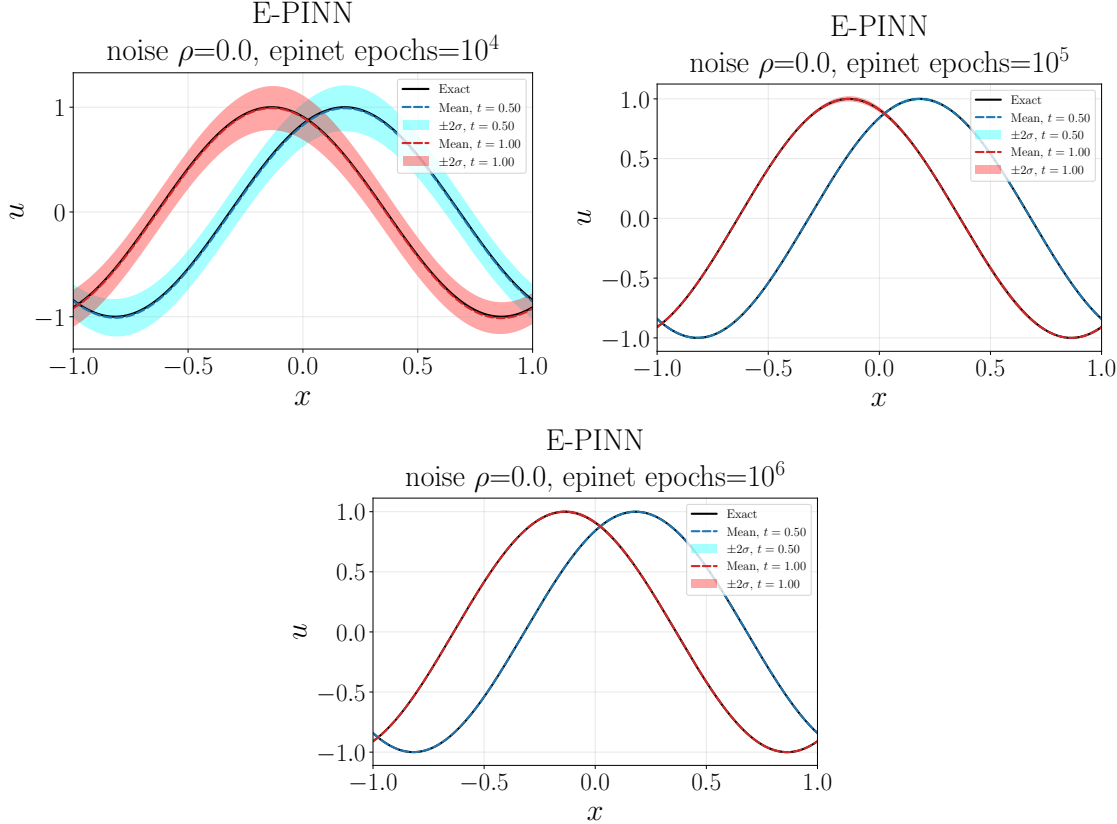


Figure 15: Effect of epinet training epochs. Shown for epinet epochs $\{10^4, 10^5, 10^6\}$. Each panel shows the predictive mean and $\pm 2\sigma$ epistemic bands for u ; all other settings are fixed across runs.

Table 8: Epinet epoch ablation: E-PINN metrics versus epinet epochs. RMSE is computed with the predictive mean μ_u . (Sharpness/time/RMSE: lower is better; coverage: higher is better.)

epinet epochs	Sharpness $\mu_{2\sigma}^w$	Coverage (95%)	RMSE	Time (s)	Time (epinet) (s)
10^4	0.39	1.00	0.0118	1248.34	275.17
10^5	0.03	1.00	0.0004	4833.58	3599.50
10^6	0.01	1.00	0.0003	28408.96	27419.18

From 10^4 to 10^5 epinet epochs (Table 8), sharpness decreases markedly and RMSE drops by an order of magnitude while coverage remains conservative (≈ 1.00). Total time increases because of the longer epinet schedule, indicating that the epinet at 10^4 epochs is under-optimized and benefits from continued training. At 10^6 epochs, bands tighten further and RMSE decreases marginally while coverage remains at 1.00. The incremental gains beyond 10^5 come at substantially higher cost, suggesting diminishing returns past 10^5 under this configuration.

3.5.4 Effect of the number of training epochs in the base network

This ablation studies the effect of the base network training budget. The configuration and data channels match the previous subsection, with the default architecture (32, 32, 32) and $N_{\text{colloc}} = 1000$. We vary only the base epochs $\{10^4, 10^5, 10^6\}$; the epinet training remains fixed to 10^4 epochs. Figure 16 shows the three cases used in the study.

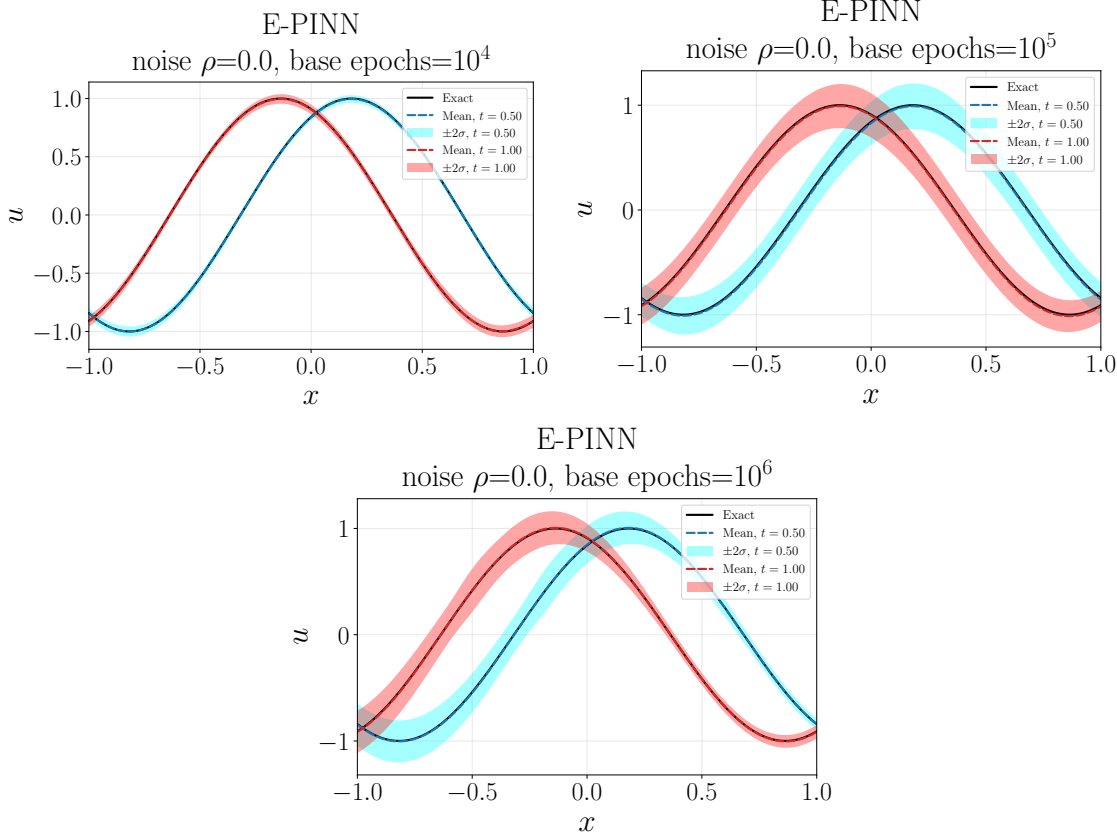


Figure 16: Effect of base training epochs. Shown for base epochs $\{10^4, 10^5, 10^6\}$. Each panel shows the predictive mean and $\pm 2\sigma$ epistemic bands for u ; epinet epochs are held fixed.

For consistency across runs, wall-clock throughput for B-PINN uses $M = 11,000$ total samples with 1,000 burn-in steps, matching the default configuration.

Table 9: Base epoch ablation: E-PINN metrics versus base epochs. RMSE is computed with the predictive mean μ_u . (Sharpness/time/RMSE: lower is better; coverage: higher is better.)

Base epochs	Sharpness $\mu_{2\sigma}^u$	Coverage (95%)	RMSE	Time (s)	Time (epinet) (s)
10^4	0.07	1.00	0.0027	718.14	285.06
10^5	0.39	1.00	0.0118	1772.63	317.59
10^6	0.29	1.00	0.0039	9541.34	313.91

With the epinet fixed at 10^4 epochs (Table 9), 10^4 base epochs produce the tightest bands and the lowest RMSE. Increasing the base budget to 10^5 inflates sharpness and error; at 10^6 the RMSE recovers while bands remain wider than at 10^4 . Total time grows with the base budget and dominates overall throughput at 10^6 . These trends suggest that, in physics-only training of the base, coupling the base schedule to the epinet schedule matters: longer base optimization can reduce the utility of the base features to the epinet under a fixed epinet budget, which the epinet expresses as wider corrections with larger variance. In this regime, relatively shorter base training paired with a fixed epinet budget yields better overall accuracy and sharper calibrated intervals.

3.5.5 Effect of interior u noise

This section studies the effect of interior measurement noise in the data augmented setting. We use three levels: $\rho \in \{0.00, 0.10, 0.30\}$, where the standard deviation is $\sigma = \rho \|u\|_\infty$. The case $\rho = 0.00$ uses physics only, and $\rho > 0$

uses physics plus noisy interior u data. All other hyperparameters are kept at their defaults. Figure 17 shows the three cases used in the study. Table 10 reports the measured metrics.

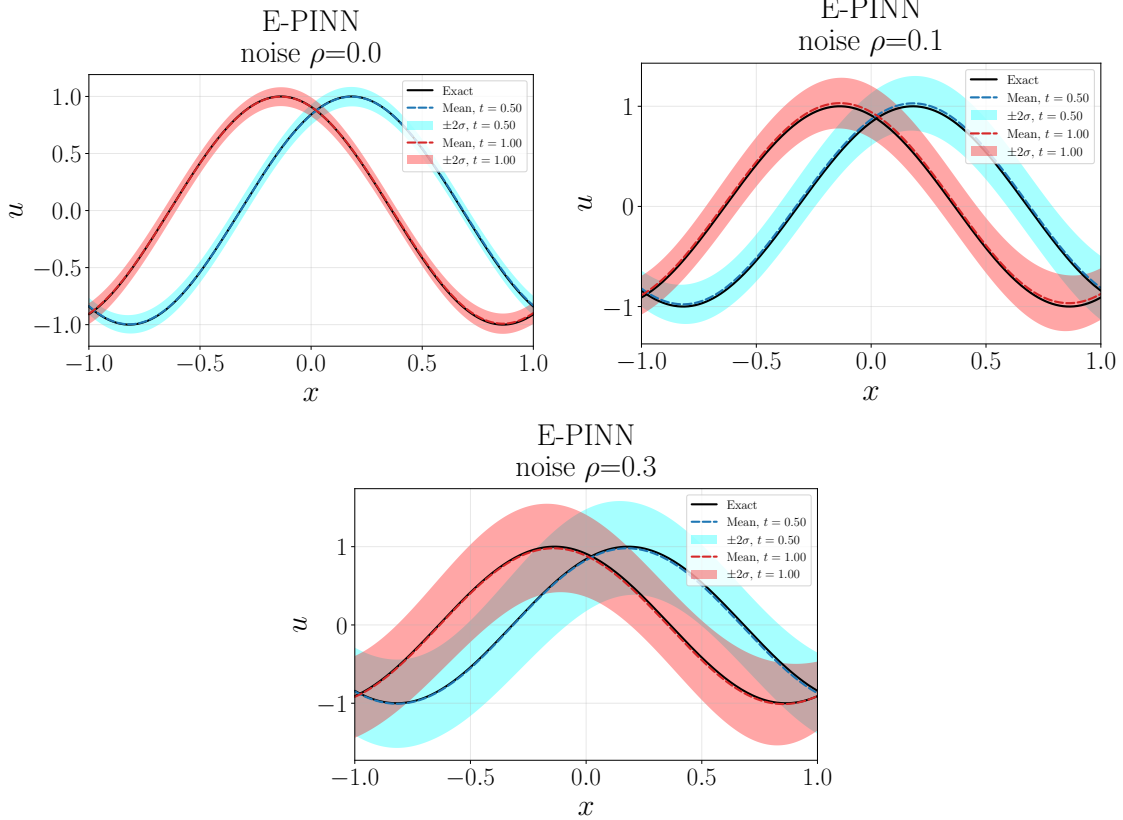


Figure 17: Effect of interior u noise. Shown for $\rho \in \{0.00, 0.10, 0.30\}$ with $\sigma = \rho \|u\|_\infty$. The case $\rho = 0.00$ uses physics only; $\rho > 0$ adds noisy interior u data. Each panel shows the predictive mean and $\pm 2\sigma$ epistemic bands for u ; other settings are fixed.

Table 10: Noise ablation: E-PINN metrics versus ρ for Burgers. RMSE is computed with the predictive mean μ_u . (Sharpness/time/RMSE: lower is better; coverage: higher is better.)

ρ	Sharpness $\mu_{2\sigma}^w$	Coverage (95%)	RMSE	Time (s)	Time (epinet) (s)
0.00	0.17	1.00	0.0046	4718.98	1303.11
0.10	0.52	1.00	0.0276	4625.84	1294.11
0.30	1.16	1.00	0.0220	5431.61	1509.17

Sharpness increases with noise while coverage remains conservative (≈ 1.00) in all cases (Table 10). RMSE increases from $\rho = 0.00$ to $\rho = 0.10$ and is lower at $\rho = 0.30$ than at $\rho = 0.10$. Under the fixed loss weights, noisier interior measurements reduce the effective information content of the data channel relative to the PDE channel. At higher noise, the optimizer leans more on the physics residual, which regularizes the mean and can yield a lower RMSE on the noiseless target, while the epinet widens the bands to preserve empirical coverage. The epinet training time is similar across noise levels (same size and epochs) and increases slightly at higher noise; total time rises at $\rho = 0.30$ due to longer base optimization.

4 Conclusions

This work introduces E-PINNs, a framework that extends physics-informed neural networks by efficiently representing epistemic uncertainty through a compact, companion epinet. The epinet is trained on stop-gradient features from a

pre-trained PINN and uses a low-dimensional epistemic index for Monte Carlo estimation. In practice, this attaches uncertainty to an existing surrogate with modest additional cost.

Extensive evaluations across forward PDE problems and an inverse problem indicate that E-PINNs produce conservative uncertainty bands with accurate means while maintaining a favorable balance between uncertainty quality and computational cost. Relative to Bayesian PINNs based on Hamiltonian Monte Carlo, E-PINNs generally achieve comparable or better accuracy at lower wall-clock times on CPU; in one inverse case B-PINN ran faster but underestimated κ (posterior mean ≈ 0.078 vs true 0.10). Compared with Dropout-PINNs, E-PINNs deliver sharper intervals with better empirical coverage under the settings tested.

Ablation studies provide guidance for practical use. Under a fixed training budget, moderate numbers of collocation points suffice to calibrate the epinet features; pushing them much higher without adjusting the schedule can widen intervals. Modest epinet capacity is effective, while substantially larger widths increase variance and error without improving coverage. Extending epinet training reduces error and tightens bands up to about 10^5 epochs, after which improvements are marginal relative to cost. With higher interior u noise, intervals widen while empirical coverage remains near nominal levels.

In summary, E-PINNs offer a computationally efficient approach to epistemic uncertainty for PINNs. The method attaches to existing surrogates with a small training overhead and performs well across the problems studied. Future work will extend E-PINNs to larger operator-learning settings and evaluate performance on experimental datasets.

5 Code and data availability

All code, trained models, and data required to replicate the examples presented in this paper will be released upon publication.

6 Acknowledgements

This project was completed with support from the U.S. Department of Energy, Advanced Scientific Computing Research program, under the "Resolution-invariant deep learning for accelerated propagation of epistemic and aleatory uncertainty in multi-scale energy storage systems, and beyond" project (Project No. 81824) and under the "Uncertainty Quantification for Multifidelity Operator Learning (MOLUcQ)" project (Project No. 81739). The computational work was performed using PNNL Institutional Computing at Pacific Northwest National Laboratory. Pacific Northwest National Laboratory (PNNL) is a multi-program national laboratory operated for the U.S. Department of Energy (DOE) by Battelle Memorial Institute under Contract No. DE-AC05-76RL01830.

Appendix

Additional 2D nonlinear Poisson figures

Figures 18 provides the $\rho = 0.10$ comparison (mean, standard deviation, and error) for completeness.

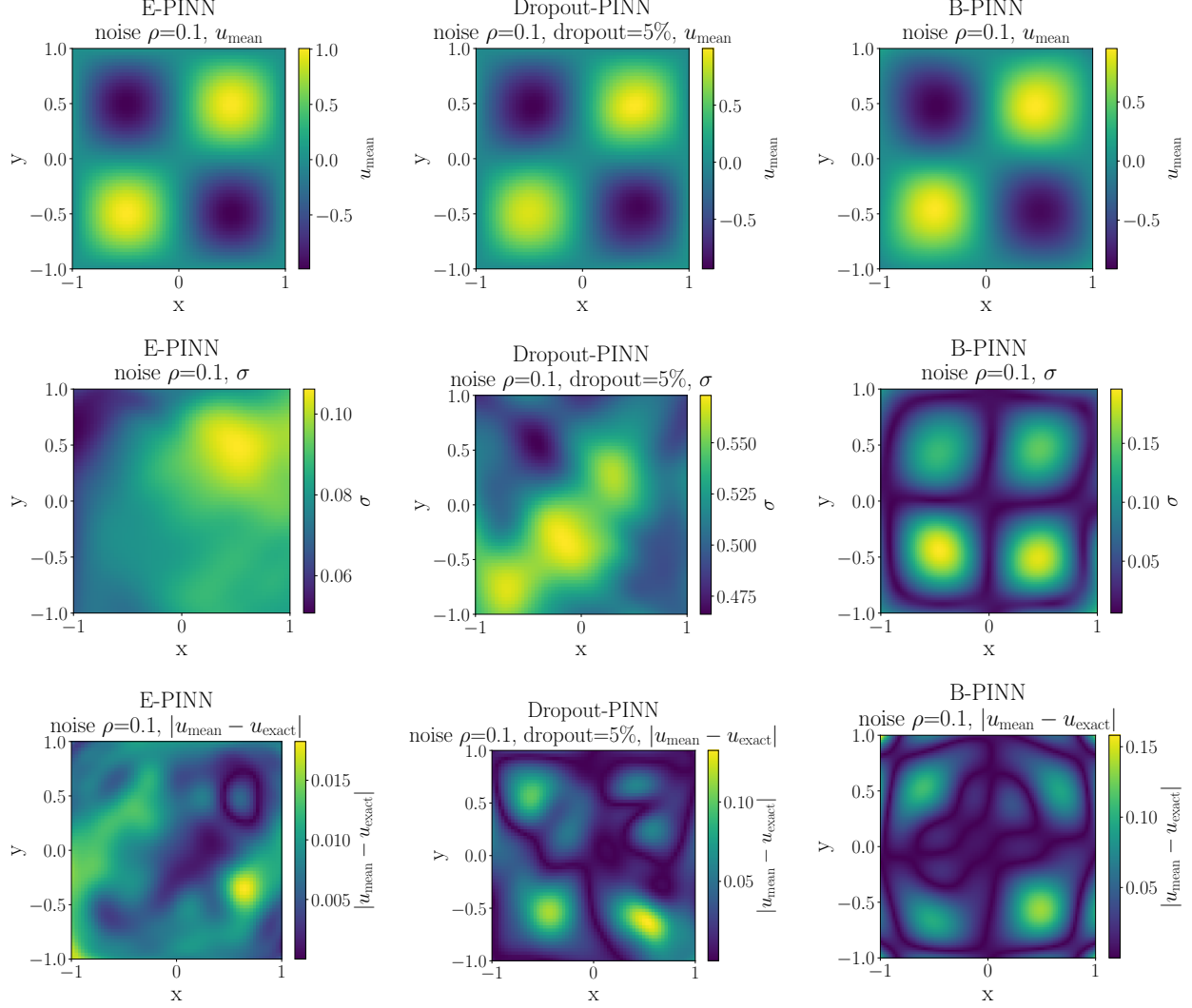


Figure 18: 2D nonlinear Poisson ($\rho = 0.10$): top, mean u ; middle, epistemic standard deviation; bottom, absolute error. Columns: E-PINN (left), Dropout-PINN (center), B-PINN (right).

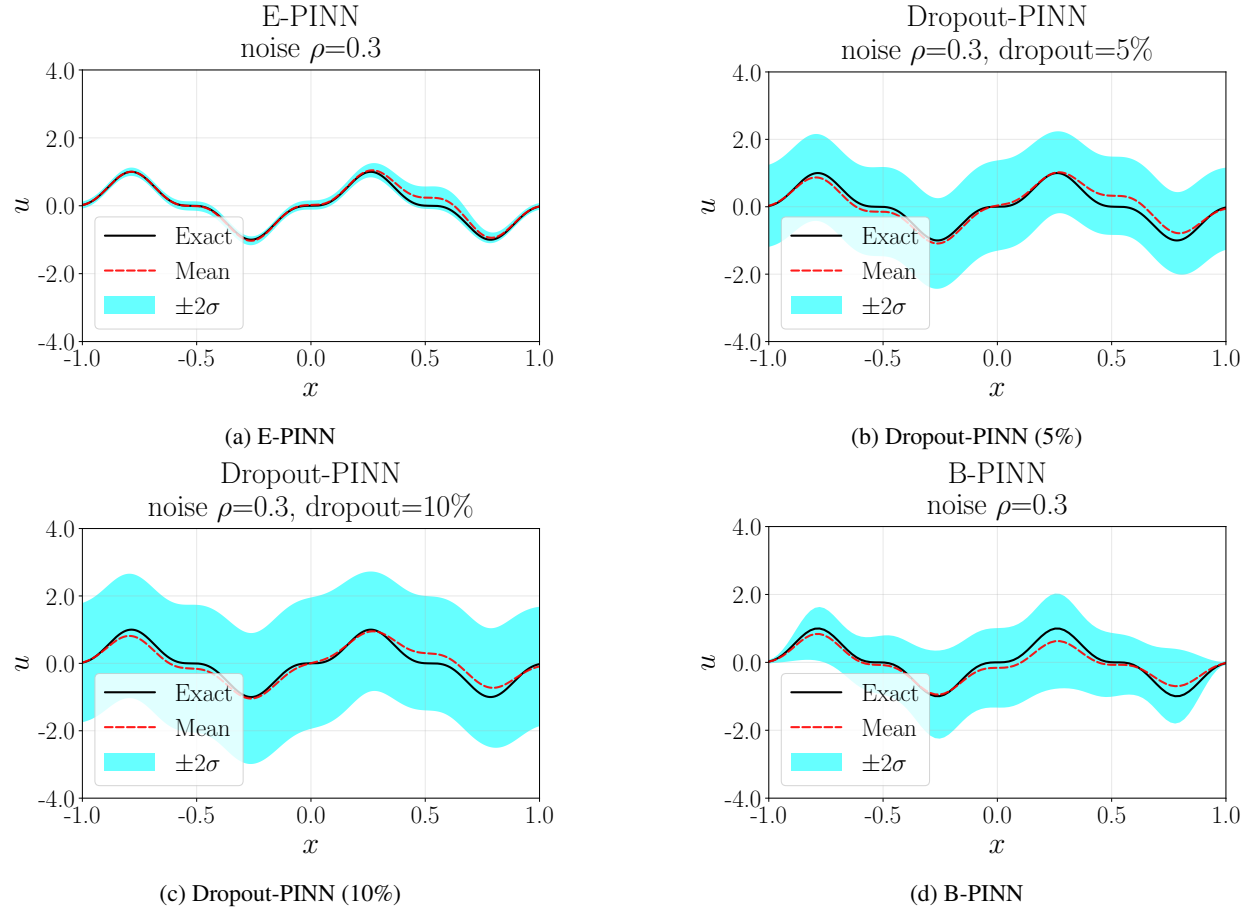
Additional 1D Poisson figures

Figure 19: 1D Poisson (Gaussian noise, $\sigma = 0.30 \|\mathbf{u}\|_\infty$): mean and $\pm 2\sigma$ epistemic bands for $u(x)$. Methods: (a) E-PINN, (b) Dropout-PINN (5%), (c) Dropout-PINN (10%), (d) B-PINN.

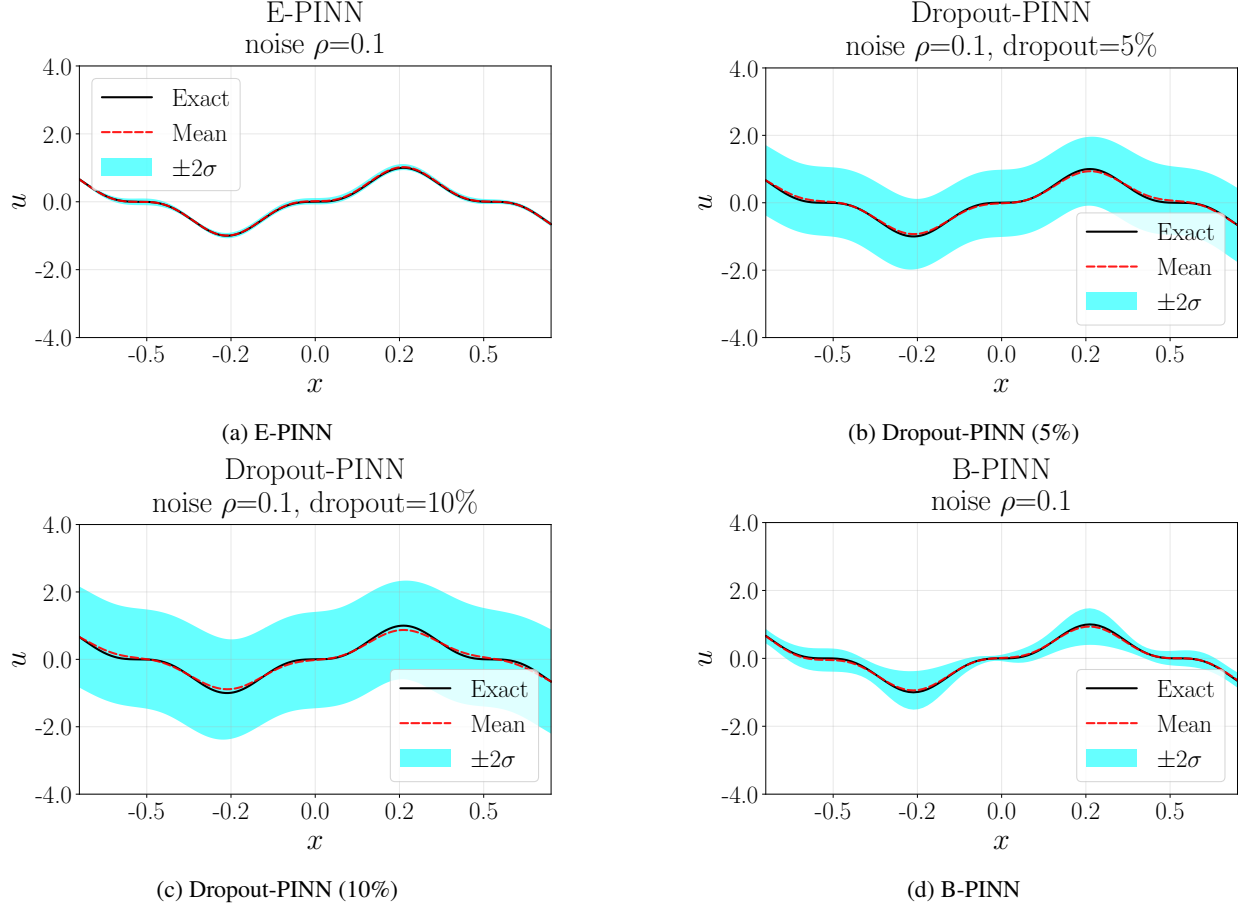
Additional 1D nonlinear Poisson figures

Figure 20: 1D nonlinear Poisson (Gaussian noise, $\sigma = 0.10 \|u\|_\infty$): mean and $\pm 2\sigma$ epistemic bands for $u(x)$. Methods: (a) E-PINN, (b) Dropout-PINN (5%), (c) Dropout-PINN (10%), (d) B-PINN.

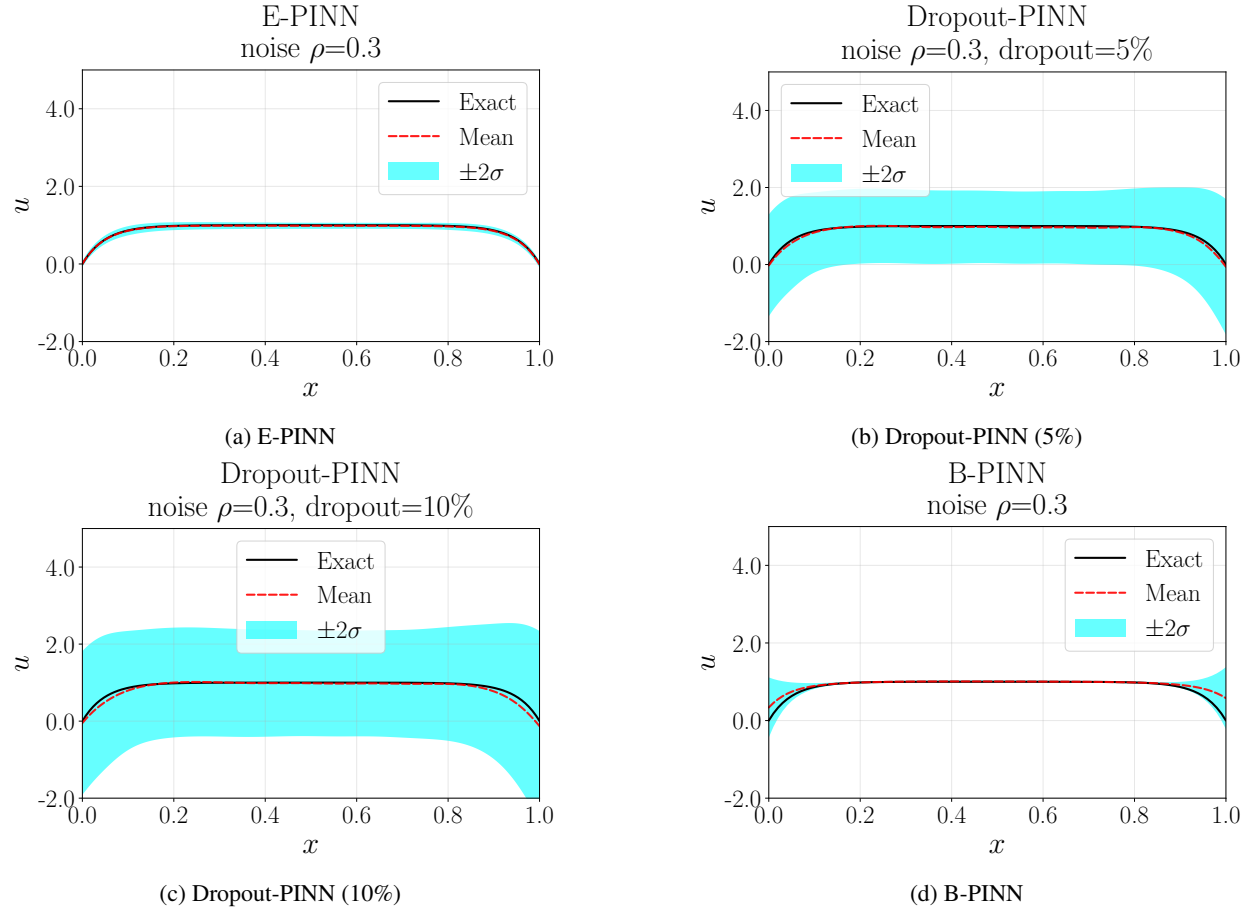
Additional 1D porous medium figures

Figure 21: 1D porous medium (Gaussian noise, $\sigma = 0.30 \|u\|_\infty$): mean and $\pm 2\sigma$ epistemic bands for $u(x)$. Methods: (a) E-PINN, (b) Dropout-PINN (5%), (c) Dropout-PINN (10%), (d) B-PINN.

Additional 1D heat equation figures

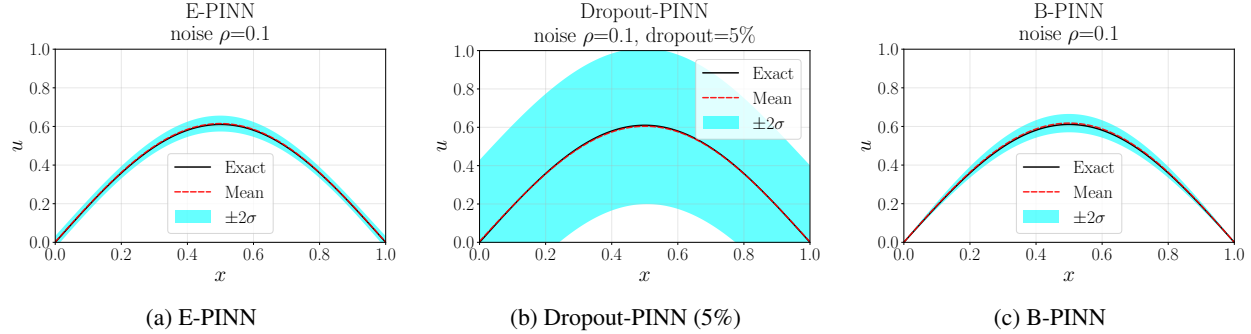


Figure 22: 1D heat equation (inverse; $\rho = 0.10$, $t = 0.50$): mean and $\pm 2\sigma$ epistemic bands for $u(x, t)$ (instantaneous slice). Methods: (a) E-PINN, (b) Dropout-PINN (5%), (c) B-PINN.

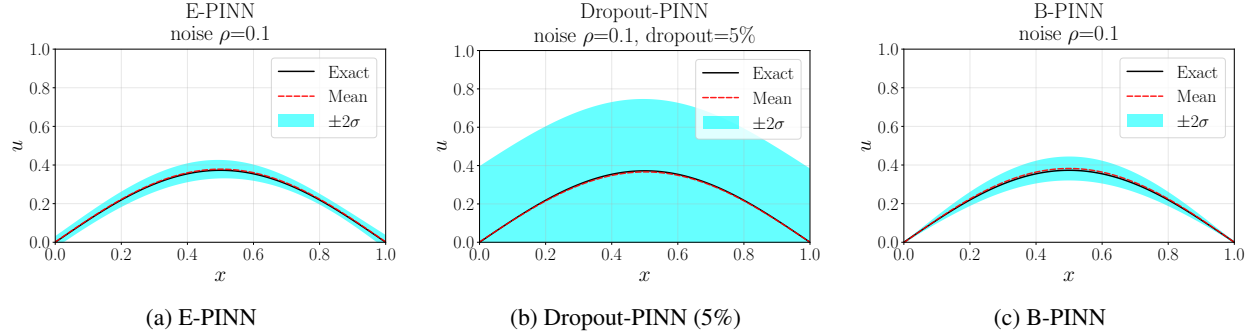


Figure 23: 1D heat equation (inverse; $\rho = 0.10$, $t = 1.00$): mean and $\pm 2\sigma$ epistemic bands for $u(x, t)$ (instantaneous slice). Methods: (a) E-PINN, (b) Dropout-PINN (5%), (c) B-PINN.

References

- [1] Maziar Raissi, Paris Perdikaris, and George E Karniadakis. Physics-informed neural networks: A deep learning framework for solving forward and inverse problems involving nonlinear partial differential equations. *Journal of Computational physics*, 378:686–707, 2019.
- [2] Xiaowei Jin, Shengze Cai, Hui Li, and George Em Karniadakis. Nsfnets (navier-stokes flow nets): Physics-informed neural networks for the incompressible navier-stokes equations. *Journal of Computational Physics*, 426:109951, 2021.
- [3] Shengze Cai, Zhiping Mao, Zhicheng Wang, Minglang Yin, and George Em Karniadakis. Physics-informed neural networks (pinns) for fluid mechanics: A review. *Acta Mechanica Sinica*, 37(12):1727–1738, 2021.
- [4] Sean Hanrahan, Melissa Kozul, and Richard D Sandberg. Studying turbulent flows with physics-informed neural networks and sparse data. *International Journal of Heat and Fluid Flow*, 104:109232, 2023.
- [5] Yusuf Patel, Vincent Mons, Olivier Marquet, and Georgios Rigas. Turbulence model augmented physics-informed neural networks for mean-flow reconstruction. *Physical Review Fluids*, 9(3):034605, 2024.
- [6] Ryno Laubscher. Simulation of multi-species flow and heat transfer using physics-informed neural networks. *Physics of Fluids*, 33(8), 2021.
- [7] Jiaxuan Xu, Han Wei, and Hua Bao. Physics-informed neural networks for studying heat transfer in porous media. *International Journal of Heat and Mass Transfer*, 217:124671, 2023.
- [8] Shengze Cai, Zhicheng Wang, Sifan Wang, Paris Perdikaris, and George Em Karniadakis. Physics-informed neural networks for heat transfer problems. *Journal of Heat Transfer*, 143(6):060801, 2021.
- [9] Darioush Jalili, Seohee Jang, Mohammad Jadidi, Giovanni Giustini, Amir Keshmiri, and Yasser Mahmoudi. Physics-informed neural networks for heat transfer prediction in two-phase flows. *International Journal of Heat and Mass Transfer*, 221:125089, 2024.
- [10] Francisco Sahli Costabal, Yibo Yang, Paris Perdikaris, Daniel E Hurtado, and Ellen Kuhl. Physics-informed neural networks for cardiac activation mapping. *Frontiers in Physics*, 8:42, 2020.
- [11] Georgios Kissas, Yibo Yang, Eileen Hwuiang, Walter R Witschey, John A Detre, and Paris Perdikaris. Machine learning in cardiovascular flows modeling: Predicting arterial blood pressure from non-invasive 4d flow mri data using physics-informed neural networks. *Computer Methods in Applied Mechanics and Engineering*, 358:112623, 2020.
- [12] Kaan Sel, Amirmohammad Mohammadi, Roderic I Pettigrew, and Roozbeh Jafari. Physics-informed neural networks for modeling physiological time series for cuffless blood pressure estimation. *npj Digital Medicine*, 6(1):110, 2023.
- [13] Arbaaz Khan and David A Lowther. Physics informed neural networks for electromagnetic analysis. *IEEE Transactions on Magnetics*, 58(9):1–4, 2022.
- [14] Marco Baldan, Paolo Di Barba, and David A Lowther. Physics-informed neural networks for inverse electromagnetic problems. *IEEE Transactions on Magnetics*, 59(5):1–5, 2023.
- [15] Liu Yang, Xuhui Meng, and George Em Karniadakis. B-pinns: Bayesian physics-informed neural networks for forward and inverse pde problems with noisy data. *Journal of Computational Physics*, 425:109913, 2021.
- [16] Armen Der Kiureghian and Ove Ditlevsen. Aleatory or epistemic? does it matter? *Structural safety*, 31(2):105–112, 2009.
- [17] Eyke Hüllermeier and Willem Waegeman. Aleatoric and epistemic uncertainty in machine learning: An introduction to concepts and methods. *Machine learning*, 110(3):457–506, 2021.
- [18] Katiana Kontolati, Dimitrios Loukrezis, Dimitrios G Giovanis, Lohit Vandana, and Michael D Shields. A survey of unsupervised learning methods for high-dimensional uncertainty quantification in black-box-type problems. *Journal of Computational Physics*, 464:111313, 2022.
- [19] Himanshu Sharma, Lukáš Novák, and Michael Shields. Physics-constrained polynomial chaos expansion for scientific machine learning and uncertainty quantification. *Computer Methods in Applied Mechanics and Engineering*, 431:117314, 2024.
- [20] David JC MacKay. A practical bayesian framework for backpropagation networks. *Neural computation*, 4(3):448–472, 1992.
- [21] Alex Graves. Practical variational inference for neural networks. *Advances in neural information processing systems*, 24, 2011.

[22] Radford M Neal. *Bayesian learning for neural networks*, volume 118. Springer Science & Business Media, 2012.

[23] Audrey Olivier, Michael D. Shields, and Lori Graham-Brady. Bayesian neural networks for uncertainty quantification in data-driven materials modeling. *Computer Methods in Applied Mechanics and Engineering*, 386:114079, 2021. ISSN 0045-7825. doi:<https://doi.org/10.1016/j.cma.2021.114079>. URL <https://www.sciencedirect.com/science/article/pii/S0045782521004102>.

[24] Charles Blundell, Julien Cornebise, Koray Kavukcuoglu, and Daan Wierstra. Weight uncertainty in neural network. In *International conference on machine learning*, pages 1613–1622. PMLR, 2015.

[25] Balaji Lakshminarayanan, Alexander Pritzel, and Charles Blundell. Simple and scalable predictive uncertainty estimation using deep ensembles. *Advances in neural information processing systems*, 30, 2017.

[26] Stanislav Fort, Huiyi Hu, and Balaji Lakshminarayanan. Deep ensembles: A loss landscape perspective. *arXiv preprint arXiv:1912.02757*, 2019.

[27] Arsenii Ashukha, Alexander Lyzhov, Dmitry Molchanov, and Dmitry Vetrov. Pitfalls of in-domain uncertainty estimation and ensembling in deep learning. *arXiv preprint arXiv:2002.06470*, 2020.

[28] Geoffrey E Hinton, Nitish Srivastava, Alex Krizhevsky, Ilya Sutskever, and Ruslan R Salakhutdinov. Improving neural networks by preventing co-adaptation of feature detectors. *arXiv preprint arXiv:1207.0580*, 2012.

[29] Yarin Gal and Zoubin Ghahramani. Dropout as a bayesian approximation: Representing model uncertainty in deep learning. In *international conference on machine learning*, pages 1050–1059. PMLR, 2016.

[30] Yarin Gal, Jiri Hron, and Alex Kendall. Concrete dropout. *Advances in neural information processing systems*, 30, 2017.

[31] Yingzhen Li and Yarin Gal. Dropout inference in bayesian neural networks with alpha-divergences. In *International conference on machine learning*, pages 2052–2061. PMLR, 2017.

[32] Takuya Hiraoka, Takahisa Imagawa, Taisei Hashimoto, Takashi Onishi, and Yoshimasa Tsuruoka. Dropout q-functions for doubly efficient reinforcement learning. *arXiv preprint arXiv:2110.02034*, 2021.

[33] Liu Yang, Dongkun Zhang, and George Em Karniadakis. Physics-informed generative adversarial networks for stochastic differential equations. *SIAM Journal on Scientific Computing*, 42(1):A292–A317, 2020.

[34] Zongren Zou, Xuhui Meng, Apostolos F Psaros, and George E Karniadakis. Neuraluq: A comprehensive library for uncertainty quantification in neural differential equations and operators. *SIAM Review*, 66(1):161–190, 2024.

[35] Dongkun Zhang, Lu Lu, Ling Guo, and George Em Karniadakis. Quantifying total uncertainty in physics-informed neural networks for solving forward and inverse stochastic problems. *Journal of Computational Physics*, 397:108850, 2019.

[36] Lu Lu, Pengzhan Jin, and George Em Karniadakis. Deepenet: Learning nonlinear operators for identifying differential equations based on the universal approximation theorem of operators. *arXiv preprint arXiv:1910.03193*, 2019.

[37] Yibo Yang, Georgios Kissas, and Paris Perdikaris. Scalable uncertainty quantification for deep operator networks using randomized priors. *Computer Methods in Applied Mechanics and Engineering*, 399:115399, 2022.

[38] Andrew Pensoneault and Xueyu Zhu. Uncertainty quantification for deepnets with ensemble kalman inversion. *Journal of computational physics*, 523:113670, 2025.

[39] Shailesh Garg and Souvik Chakraborty. Vb-deepenet: A bayesian operator learning framework for uncertainty quantification. *Engineering Applications of Artificial Intelligence*, 118:105685, 2023.

[40] Zecheng Zhang, Christian Moya, Wing Tat Leung, Guang Lin, and Hayden Schaeffer. Bayesian deep operator learning for homogenized to fine-scale maps for multiscale pde. *Multiscale Modeling & Simulation*, 22(3):956–972, 2024.

[41] Lena Podina, Mahdi Torabi Rad, and Mohammad Kohandel. Conformalized physics-informed neural networks. *arXiv preprint arXiv:2405.08111*, 2024.

[42] Christian Moya, Amirhossein Mollaali, Zecheng Zhang, Lu Lu, and Guang Lin. Conformalized-deepenet: A distribution-free framework for uncertainty quantification in deep operator networks. *Physica D: Nonlinear Phenomena*, 471:134418, 2025.

[43] Anastasios Angelopoulos, Stephen Bates, Jitendra Malik, and Michael I Jordan. Uncertainty sets for image classifiers using conformal prediction. *arXiv preprint arXiv:2009.14193*, 2020.

[44] Ian Osband, Zheng Wen, Seyed Mohammad Asghari, Vikrant Dwaracherla, Morteza Ibrahimi, Xiuyuan Lu, and Benjamin Van Roy. Epistemic neural networks. *Advances in Neural Information Processing Systems*, 36:2795–2823, 2023.

- [45] Xuhui Meng, Hessam Babaee, and George Em Karniadakis. Multi-fidelity bayesian neural networks: Algorithms and applications. *Journal of Computational Physics*, 438:110361, 2021.
- [46] Guang Lin, Yating Wang, and Zecheng Zhang. Multi-variance replica exchange sgmcemc for inverse and forward problems via bayesian pinn. *Journal of Computational Physics*, 460:111173, 2022.
- [47] Andrew Pensoneault and Xueyu Zhu. Efficient bayesian physics informed neural networks for inverse problems via ensemble kalman inversion. *Journal of Computational Physics*, 508:113006, 2024.
- [48] Nitish Srivastava, Geoffrey Hinton, Alex Krizhevsky, Ilya Sutskever, and Ruslan Salakhutdinov. Dropout: a simple way to prevent neural networks from overfitting. *The journal of machine learning research*, 15(1):1929–1958, 2014.
- [49] Jiayu Yao, Weiwei Pan, Soumya Ghosh, and Finale Doshi-Velez. Quality of uncertainty quantification for bayesian neural network inference. *arXiv preprint arXiv:1906.09686*, 2019.
- [50] Levi D McCleny and Ulisses M Braga-Neto. Self-adaptive physics-informed neural networks. *Journal of Computational Physics*, 474:111722, 2023.
- [51] Sokratis J Anagnostopoulos, Juan Diego Toscano, Nikolaos Stergiopoulos, and George Em Karniadakis. Residual-based attention in physics-informed neural networks. *Computer Methods in Applied Mechanics and Engineering*, 421:116805, 2024.
- [52] Wenqian Chen, Amanda A Howard, and Panos Stinis. Self-adaptive weights based on balanced residual decay rate for physics-informed neural networks and deep operator networks. *arXiv preprint arXiv:2407.01613*, 2024.
- [53] Tilman Gneiting, Fadoua Balabdaoui, and Adrian E Raftery. Probabilistic forecasts, calibration and sharpness. *Journal of the Royal Statistical Society Series B: Statistical Methodology*, 69(2):243–268, 2007.
- [54] Tim Pearce, Alexandra Brintrup, Mohamed Zaki, and Andy Neely. High-quality prediction intervals for deep learning: A distribution-free, ensembled approach. In *International conference on machine learning*, pages 4075–4084. PMLR, 2018.
- [55] Abbas Khosravi, Saeid Nahavandi, Doug Creighton, and Amir F Atiya. Comprehensive review of neural network-based prediction intervals and new advances. *IEEE Transactions on neural networks*, 22(9):1341–1356, 2011.
- [56] LH Yu and CY Wang. Darcy-brinkman flow through a bumpy channel. *Transport in porous media*, 97(3):281–294, 2013.
- [57] Nicos S Martys. Improved approximation of the brinkman equation using a lattice boltzmann method. *Physics of fluids*, 13(6):1807–1810, 2001.